



**VICTORIA UNIVERSITY**  
MELBOURNE AUSTRALIA

*Design of prefabricated footing connection using a coupled hydro-mechanical finite element model*

This is the Published version of the following publication

Teodosio, Bertrand, Baduge, Kasun Shanaka Kristombu and Mendis, Priyan (2021) Design of prefabricated footing connection using a coupled hydro-mechanical finite element model. *Structural Concrete*, 23 (5). pp. 2669-2695. ISSN 1464-4177

The publisher's official version can be found at  
<https://onlinelibrary.wiley.com/doi/10.1002/suco.202100315>  
Note that access to this version may require subscription.

Downloaded from VU Research Repository <https://vuir.vu.edu.au/45142/>

## ARTICLE

# Design of prefabricated footing connection using a coupled hydro-mechanical finite element model

Bertrand Teodosio<sup>1</sup>  | Kasun Shanaka Kristombu Baduge<sup>2</sup>  | Priyan Mendis<sup>2</sup>

<sup>1</sup>Institute of Sustainable Industries and Liveable Cities, Victoria University, Footscray, Victoria, Australia

<sup>2</sup>Department of Infrastructure Engineering, The University of Melbourne, Parkville, Victoria, Australia

## Correspondence

Bertrand Teodosio, Institute of Sustainable Industries and Liveable Cities, Victoria University, D668D/E 70/104 Ballarat Rd, Footscray, VIC 3011, Australia.

Email: [bertrand.teodosio@vu.edu.au](mailto:bertrand.teodosio@vu.edu.au)

## Funding information

Australian Research Council, Grant/Award Number: IC150100023

## Abstract

The use of prefabricated systems can alleviate the inadequate housing and skilled workers in most developed countries by expediting required construction time, reducing material wastage, decreasing the effect of weather impacts, minimizing unexpected costs, skilled labor dependence, and construction hazards. The full potential of prefabricated construction is yet to be realized in part due to most advancements being focused on its superstructure. The development of prefabricated substructures for lightweight buildings needs to consider the susceptibility to damage induced by the shrink-swell movement of expansive soils causing significant global financial losses. Prefabricated substructures should have robust connections in discontinued regions to transfer forces and moments. Due to these issues, the aim of this study is to develop a connection for prefabricated raft substructures of single-detached dwellings on expansive soils using a combined soil-structure contact analysis and strut-and-tie model approach. The developed substructure system was validated using experiments and further investigated through numerical simulations. The developed prefabricated connection was observed to have satisfactory performance, potentially overcoming most construction limitations of conventional monolithic cast-in-place raft substructures, such as faster, safer, and more sustainable construction, while providing comparable strength and serviceability.

## KEYWORDS

finite element analysis, prefabricated footing connection, reactive soils, soil-structure interaction, strut-and-tie model, topology optimization

Discussion on this paper must be submitted within two months of the print publication. The discussion will then be published in print, along with the authors' closure, if any, approximately nine months after the print publication.

This is an open access article under the terms of the [Creative Commons Attribution](https://creativecommons.org/licenses/by/4.0/) License, which permits use, distribution and reproduction in any medium, provided the original work is properly cited.

© 2021 The Authors. *Structural Concrete* published by John Wiley & Sons Ltd on behalf of International Federation for Structural Concrete.

## 1 | INTRODUCTION

Most developed countries are in the course of addressing housing affordability crisis due to increase in the demand of dwellings and shortage in the supply of skilled labor.<sup>1–5</sup> The

foremost solution of the construction industry has been to minimize labor requirements to build single-detached dwellings through automation and industrialization. Prefabricated construction, the method of building ex-situ and then transporting and assembling in-situ, is a promising construction technique requiring minimum manual labor and shorter construction period.<sup>6</sup> This technique further improves occupational health and safety of site workers, quality of built structural elements, and sustainability of building designs.<sup>7,8</sup> Significant innovations in the design and construction of prefabricated superstructures have been observed; contrarily, footings still use the traditional cast-in-place method prone to construction delay and reduced quality due to weather impact and other uncontrollable factors.<sup>9–13</sup> Prefabrication of footings has the potential to improve residential construction that are necessary to be expeditiously completed, which may alleviate the concurrent shortages of housing and skilled labour.<sup>14</sup>

Assessment of discontinued regions is essential to design a functional prefabricated substructure. Discontinued systems exposed to reactive soils undergoing substantial changes in volume dependent on changing soil moisture levels should further be evaluated since this may have detrimental impact to substructures.<sup>9</sup> The design of discontinued regions of prefabricated footings does not follow the linear strain distribution of the Bernoulli hypothesis when regions are proximate to concentrated loads, corners, bends, openings, and other discontinuities.<sup>15,16</sup> The internal flow of forces in these regions can be described using a method called strut-and-tie model (STM).<sup>17,18</sup> STM visualizes discontinued regions or D-regions using struts representing the compressive stress flow in the concrete and ties representing the tensile stress flow requiring steel reinforcements.<sup>19</sup> STM, even though based on rational premise, can be considered as an approximated approach with undefined correctness dependent on the bearing conditions of the support and the location of applied concentrated loads.<sup>20,21</sup> Thus, it is necessary to consider the effect of shrink-swell ground movements induced by reactive soils to prefabricated structures given that compressive flow and tensile flow may change due to the added or reduced pressure induced by shrinking and swelling soil.<sup>22,23</sup> These shrink-swell movements are caused by the change in soil water level between normal seasonal changes and other abnormal moisture conditions such as root water uptake of vegetation, water ponding, and pipe leakage.<sup>24–27</sup> The magnitude of differential shrink-swell movements is dependent on soil properties, environmental factors, and stress conditions, which may lead from minor to severe structural damage.<sup>28,29</sup>

Connections for discontinued regions of prefabricated raft footings are challenging to design since these are one of the most critical component in structural elements.<sup>30</sup> Designs of slab–slab connections and beam–beam

connections are prime considerations to effectively transfer shear forces and moments, and for some instances axial and torsion, to obtain the required strength and ductility requirements of prefabricated raft footings. A number of slab–slab connections and beam–beam connections for prefabricated suspended elements using bolting, in-situ grouting of reinforcing bars or dowel pins, and welding have been developed in the past years. International Federation for Structural Concrete<sup>31</sup> discussed different methods to connect slab structures, including suspended slab-slab transverse load distribution, using longitudinal shear keys and shear transfer mechanism in keyed joints of hollowed slabs using compression strut. Building and Construction Authority<sup>32</sup> suggested details for connections between suspended precast floor elements and supporting structures using wet joints either with prefabricated concrete full slab, half slab or pour strip. Stupre<sup>33</sup> developed suspended beam-beam connections mainly using tie-rods, high-tensile bolts, and welds. Among the connection methods discussed, threaded or regular bolts are the most straightforward, however, requires strict tolerance.<sup>31</sup> In-situ grouting generally requires moderate tolerance with additional protection against fire and corrosion, though to some extent dependent to weather. Welding of joints can conventionally be bonded without known tolerance issues nonetheless strenuously skill-dependent and highly weather-dependent. Although significant improvement in suspended prefabricated slabs and beams have been achieved, designing prefabricated footings of lightweight buildings ought to have additional considerations due to cyclic shrink-swell ground movements.<sup>34</sup>

The investigation of the impact of reactive soils to footings has been satisfactorily analyzed through finite element method. Fraser and Wardle<sup>35</sup> improved Winkler springs and coupled springs presented in the Lytton Method through a semi-infinite elastic configuration and afterward analyzed through iteration using the assumed soil mounds proposed by the Walsh Method. The study of Holland et al.<sup>36</sup> enhanced the method of Fraser and Wardle<sup>35</sup> through incorporating numerical simulations based on collected field data, recognized as the Swinburne Method; however, the applicability of this method may be limited to specific slab lengths, vertical soil displacement, and separation between soils and substructures due to the empirical derivation. Poulos<sup>37</sup> adopted the assumption of shapes of soil heaving using the Lytton Method<sup>38</sup> using an elastic soil continuum with strip footings constructed on the founding soil. The study of Sinha et al.<sup>39</sup> conducted simulations with varying slab sections in relation to free soil heaving based on the Lytton Method. Li<sup>40</sup> created a hydro-mechanical model using coupled thermal diffusion, thermal expansion, and mechanical deformation to mimic the fluid diffusion equation and shrink-swell indices of expansive soils. The paper of Totoev and Kleeman<sup>41</sup> suggested a model for fluid infiltration to estimate soil

suction distribution. A number of studies proposed three-dimensional decoupled soil–structure interaction (SSI) models to calculate for the volume changes caused by changes in soil matric suction.<sup>42–45</sup> Few design methods were proposed for raft footings based on finite element numerical simulations.<sup>22,46</sup> Coupled hydro-mechanical models were developed as well, where historic weather and vegetation data are required as inputs for the calculation of soil mound movements and substructure deflections. Despite the fact that these models have higher accuracy, the required inputs are often not readily available for footing designers.<sup>23,47–50</sup> Teodosio et al.<sup>51</sup> and Weerasinghe et al.<sup>52</sup> proposed a more pragmatic approach using a coupled hydro-mechanical model based on typical soil suction changes and active depth zone ( $H_s$ ), which is the depth where most of the soil movement occurs.

Thorough review of connections for prefabricated substructure was found to be insubstantial compared to connections for superstructure systems, such as suspended slabs and suspended beams. Thus, the main objective of this paper is to design the discontinued regions (D-regions) in prefabricated footings considering the pressure due to swelling soil and the absence of support due to shrinking soil. Specific objectives were laid out to achieve the research aim shown in Figure 1. The first objective is to determine the optimum material layout using SSI, topology optimization (TO), and STM. The second objective is to determine the applicable configuration of the bolt connection through numerical simulations. The third objective is to perform a comparison between the prefabricated raft footing with the developed connection and a monolithic cast-in-place waffle pod raft. The prefabricated footing was compared to a waffle pod raft since both systems are designed to be installed or constructed on-ground.

## 2 | METHODOLOGY

The methodology of this study requires an inter-disciplinary approach, presented in Figure 2. For the SSI analysis using

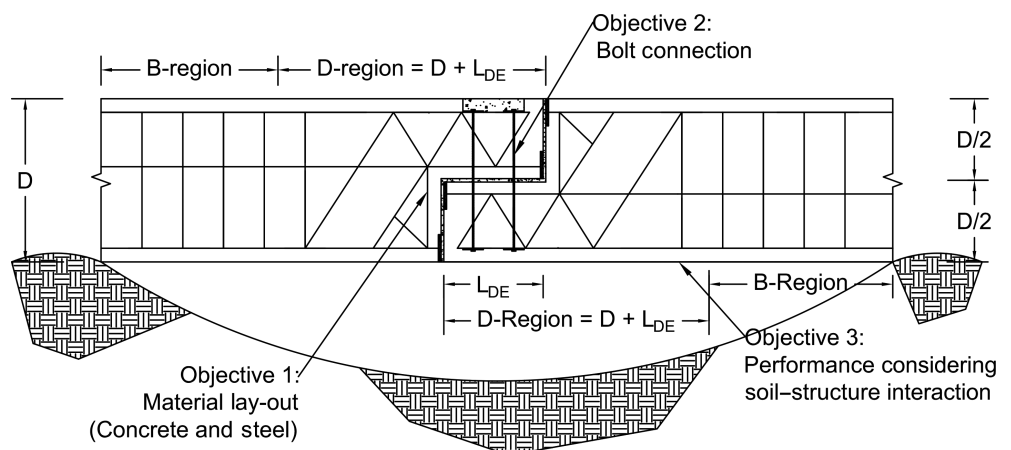
Teodosio et al.,<sup>51</sup> the unsaturated flow of fluid in a soil medium and mechanical behavior of both reinforced concrete substructures and variably saturated soil should be considered. The permeability of reactive soils affects the changes in soil saturation ( $S$ ), soil suction ( $\psi_w$ ), and soil strain ( $\epsilon$ ) inducing both ground movement and structural deformation. The concurrent change in soil moisture level and soil mechanical movement prompts contact pressure to footings altering the flow of forces being experienced by the footing system. Simulations using SSI analysis with soil support was compared to simulations disregarding the influence of soil, referred to as block-support. The C and T flows of the physical-based SSI analyses were also compared to the stochastic TO method to obtain the “optimum” material layout that will be used as the STM. The simulated peak load ( $V_u$ ) of the dapped-end beam (DEB) with the obtained optimum material layout was compared to the simulated and experimental  $V_u$  of the DEB designed by Mata-Falcón et al.<sup>53</sup> The configuration of the bolt connection (i.e., bolt size and bolt spacing) was then determined using parametric simulations. Subsequently, the performance of the designed prefabricated footing system considering SSI was simulated and compared to a monolithic waffle pod raft. The methods used in this study are the SSI, TO, and STM.

### 2.1 | SSI model

The model to simulate the shrink-swell movements of reactive soils and induced movements to footings causing deformation was based on Teodosio et al.<sup>51</sup> A reactive soil mass is modeled as a three-phase elastic material to analyze an unsaturated porous medium. The soil mass consists of solid grains of soil, wetting fluid (i.e., pore water), and nonwetting fluid (i.e., pore air).<sup>54,55</sup> The incremental coupled hydro-mechanical constitutive stress–strain law was taken as<sup>51,56</sup>

$$d\sigma' = E \left[ d\epsilon_{es} d\sigma + \left( d\epsilon_{ms} \frac{dS}{d\psi_w} d\psi_w \right) \right], \quad (1)$$

**FIGURE 1** Specific objectives of this study. D-region is the discontinued region, B-region is the region where Bernoulli–Euler Beam Theory applies,  $D$  is the depth of the beam and  $L_{DE}$  is the length of the dapped-end. D-region was assumed to be constant, which is equal to the sum of  $D$  and  $L_{DE}$  based on Schlaich and Schafer<sup>17</sup>



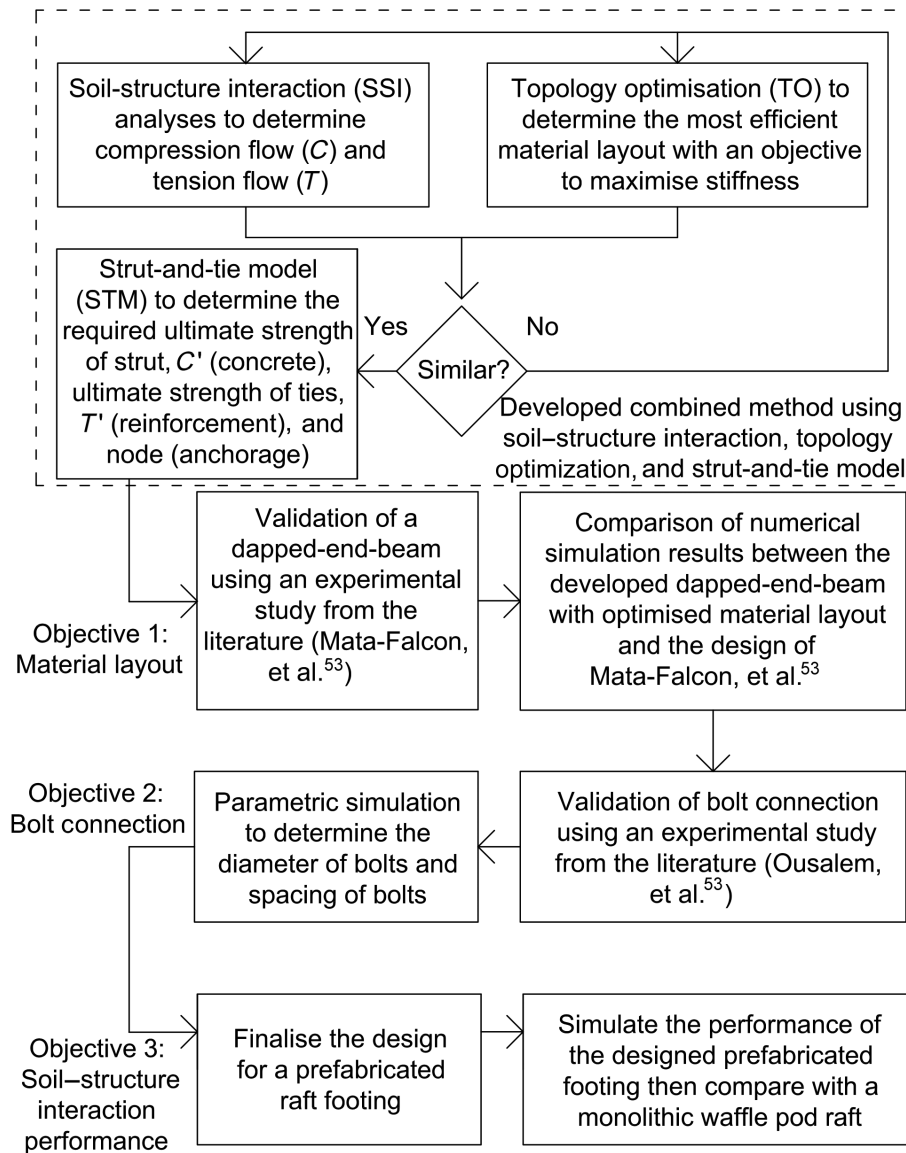


FIGURE 2 Methodology of this study

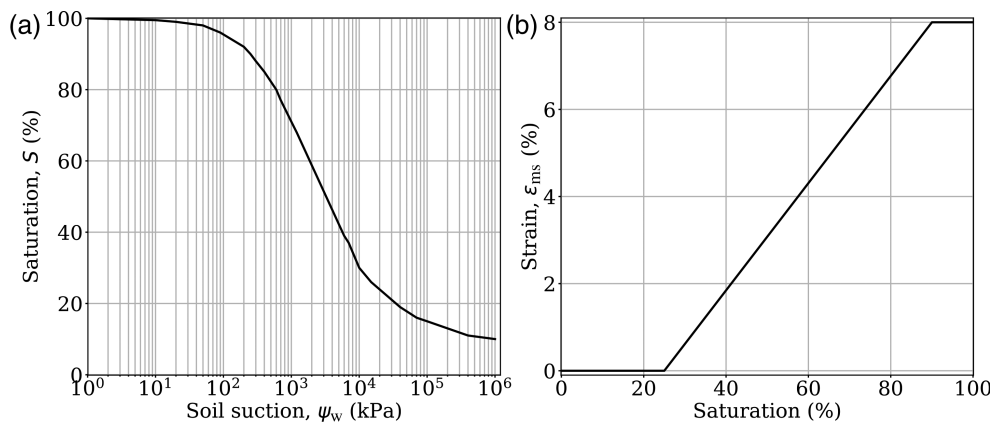


FIGURE 3 Soil material property inputs for (a) soil-water characteristic curve (SWCC) or sorption curve ( $\psi_w$  vs.  $S$ ) and (b) moisture-swelling curve or shrink-swell curve ( $\epsilon_{ms}$  vs.  $S$ ) based on the idealization of Shams et al.<sup>48</sup>

where  $\sigma$  is the effective stress,  $E$  is the tensor of elastic constants of the soil,  $S$  is the degree of soil saturation,  $\psi_w$  is the soil suction,  $\epsilon_{es}$  is the volumetric strain driven by soil effective stress, and  $\epsilon_{ms}$  is the volumetric strain

dependent on the saturation-moisture swelling relationship. The time-dependent  $\epsilon_{ms}$  can then be determined using the moisture swelling model presented in Figure 3b dependent to the corresponding  $S$ .

Numerical simulations of reinforced concrete elements (i.e., concrete beams, concrete slabs, and raft footings) subjected to applied mechanical loads considered the plastic nonlinear structural damage using Concrete Damaged Plasticity (CDP) model.<sup>57</sup> This plastic model assumes that the primary failure mechanisms are tensile cracking and compressive crushing. Deterioration of concrete occurs when unloading from any point on the strain softening plastic regime is performed, as shown in Figure 4.

The detailed hydromechanical model is further discussed in Appendix A and presented in Teodosio et al.<sup>51</sup>

Further details of the CDP model used is described in Appendix B.

## 2.2 | Topology optimization

The concept of TO distributes the material layout effectively in a given design domain dependent on given configurations of boundary conditions, applied loads, and other design and manufacturing constraints. The Solid Isotropic Microstructures with Penalisation (SIMP) Method was used in determining the optimum strut-and-

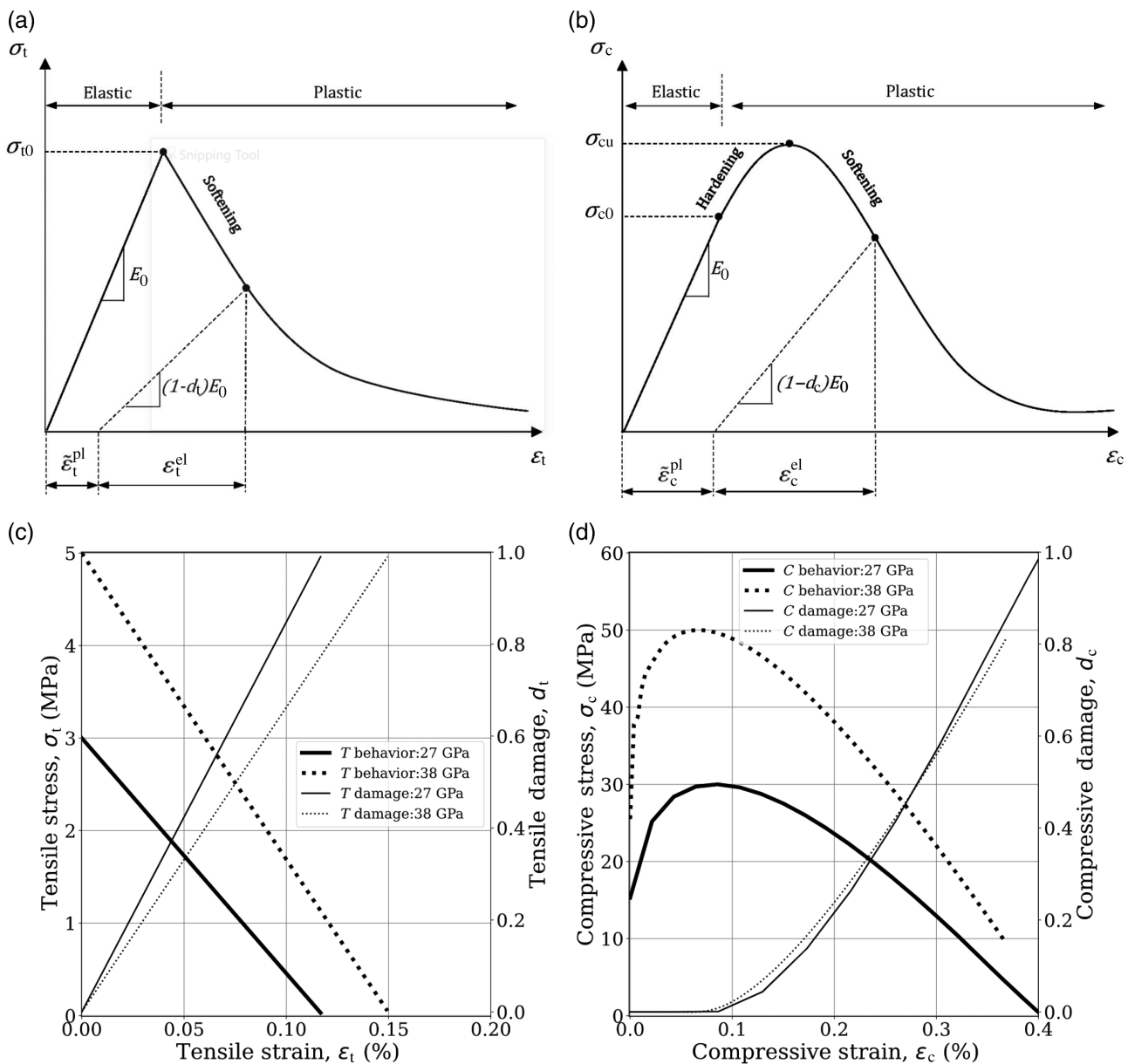


FIGURE 4 Response of concrete using Concrete Damaged Plasticity (CDP) model to (a) uniaxial loading in tension and (b) uniaxial loading in compression adapted from Teodosio.<sup>58</sup> CDP model inputs for (c) tensile plastic behavior and damage factors and (d) compressive plastic behavior and damage factors from Teodosio et al.<sup>51</sup> and Hafezolghorani et al.<sup>59</sup>

tie configuration through a stochastic approach.<sup>60–62</sup> The basic concept of SIMP Method is penalizing and removing gray elements to obtain black elements, signifying presence of material, and white elements, signifying absence of material, to form the optimum material layout. The SIMP Method used in this study was a revised version of the code proposed by Andreassen et al.,<sup>60</sup> Prasad,<sup>61</sup> and Sigmund<sup>63</sup> using MATLAB. This MATLAB code was proposed as a function described as

$$top(nelx, nely, xv, yv, volfrac, penal, rmin), \quad (2)$$

where  $nelx$  is the number of elements in the horizontal direction,  $nely$  is the number of elements in the vertical direction,  $xv$  and  $yv$  define the void in the design domain,  $volfrac$  is the volume of fraction of solids in the final iteration,  $penal$  is the penalizing power, and  $rmin$  is the filter size.

Two scenarios were considered for the optimization with an objective to maximize stiffness. The first scenario involved a DEB with reduced section at the top right portion of the structural element denoted as bottom dapped end beam or  $DEB_B$  (Figure 5a).  $DEB_B$  had values of 240 and 90 for  $nelx$  and  $nely$ , respectively. The horizontal void elements of  $DEB_B$  were from the 100th to the 240th and vertical void elements were from the 1st to the 45th. The boundary support was fixed at the left side having an undapped section, which is approximately the length of the D-region shown in Figure 1. The D-region was assumed to be constant, which is equal to the sum of  $D$  and  $L_{DE}$  based on Schlaich and Schafer.<sup>17</sup> A downward concentrated load was applied at the rightmost end of the dapped portion. The second scenario involved a DEB with reduced section at the bottom right portion of the structural element denoted as top dapped end beam or  $DEB_T$  (Figure 5b).  $DEB_T$  had values of 240 and 90 for  $nelx$  and  $nely$ , respectively. The horizontal void elements of  $DEB_T$  were from the 100th to the 240th and vertical void elements were from the 46th to the 90th. The boundary

support was fixed at the left side having an undapped section, similar with  $DEB_B$ . A downward concentrated load was applied at the rightmost end of the dapped portion. The values of  $volfrac$ ,  $penal$ , and  $rmin$  for both scenarios were 0.075, 2.5, and 1.6 based on trial and error. The input for the  $DEB_B$  is described as

$$top(240, 90, (100 : 240), (1 : 45), 0.075, 2.5, 1.6), \quad (3)$$

and the input for the  $DEB_T$  was

$$top(240, 90, (100 : 240), (46 : 90), 0.075, 2.5, 1.6), \quad (4)$$

that is shown in Figure 5a,b, respectively.

### 2.3 | Strut-and-tie model

STMs divide structural members into regions where beam theory is valid, referred to as B-regions, and where strain distribution becomes nonlinear due to geometric and load discontinuities, referred to as D-regions.<sup>17,64</sup> D-regions do not follow the linear strain distribution of the Bernoulli-Euler Beam Theory, assuming plane sections remain plane and that deformed beam slopes are small, caused by proximity to concentrated loads, corners, bends, openings, and other discontinuities.<sup>15,16</sup> The internal flow of forces in D-regions can be represented using compressive struts, representing the flow of compressive stresses in the concrete, and tension ties, representing steel reinforcements intersecting at specific nodal zones.<sup>18,19</sup>

STMs were based on rational premise although different models can be developed for varying stress distributions dependent on the bearing conditions of the support and the location of applied loads.<sup>20,21</sup>

In line with the design philosophy of Australian Standards (AS) 3600,<sup>65</sup> the required ultimate strength of struts and ties are assessed. The required ultimate tensile design strength of steel ties,  $T'$ , is determined using<sup>66</sup>

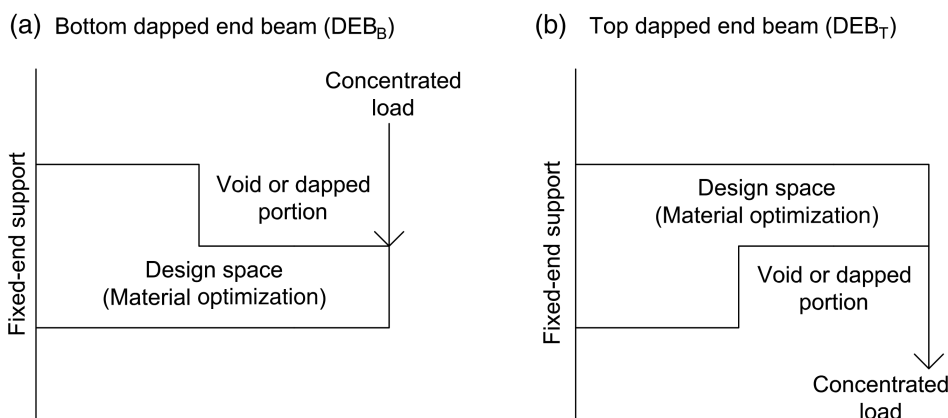


FIGURE 5 Topology optimization configuration of (a) bottom dapped end beam or  $DEB_B$  and (b) top dapped end beam or  $DEB_T$

$$T' = \phi_v A_{st} f_{sy}, \quad (5)$$

where  $\phi_v$  is the strength reduction factor,  $A_{st}$  is the area of tensile reinforcements, and  $f_{sy}$  is the yield strength of steel reinforcements.

The ultimate design strength of concrete struts,  $C'$ , can be calculated as<sup>67</sup>

$$C' = w_n \phi_v f_{cu} B = w_n \phi_v 0.9 \beta_s f'_c B, \quad (6)$$

where  $w_n$  is the width of nodal zone,  $f_{cu}$  is taken as 0.85  $f'_c$ ,  $f'_c$  is the compressive strength of concrete at 28 days and  $B$  is the width of the beam. The factor  $\beta_s$  accounts for the effect of cracking and confining reinforcements of struts.

### 3 | NUMERICAL SIMULATIONS

Numerical simulations were solved using Abaqus CAE—SIMULIA™ by Dassault Systèmes<sup>68</sup> (Ver. 2016; <https://www.3ds.com/>). Three sets of numerical simulations were performed to develop a connection for prefabricated substructure. The first set of simulations investigated the effect of supports to the compressive flow path ( $C$ ) and tensile flow path ( $T$ ) affecting the STM for the development of a prefabricated substructure connection. The second set simulated and optimized the developed DEB and bolt connection. The third set of simulations compared the behavior between a prefabricated substructure, with the developed precast connection, and a monolithic cast-in-place waffle pod raft.

#### 3.1 | Investigation of the effect of supports

Parametric simulations were performed by varying the location of supports and applied concentrated loads to determine an optimum STM. These simulations obtained  $C$  and  $T$  that will determine the required STM for swelling scenario and shrinking scenario. The parametric simulations were divided into two. First, simulations that neglect the presence and absence of soil pressure influencing the substructure, referred to as “block-support” (Figure 6a). Second, simulations that consider the effect of the applied soil pressure due to shrink-swell ground movements using the developed coupled hydromechanical model by Teodosio et al.,<sup>51</sup> referred to as “soil-support” (Figure 6b). These simulations highlight the difference of obtained  $C$  and  $T$ , between an approach neglecting the soil pressure due to shrink-swell ground

movements and an approach considering the effect of soil pressure induced by reactive soil movements.

#### 3.1.1 | Block-support simulations

Parametric simulations were performed by varying the location of supports and applied concentrated load onto two connected DEBs. The considered prefabricated slab substructure was based on a dapped waffle pod raft section with a depth ( $D$ ) of 600 mm, a beam width ( $B$ ) of 250 mm, and the notch of the DEB ( $L_{DE}$ ) was 350 mm, comparable to that of Mata-Falcón et al.<sup>53</sup> The longitudinal length ( $L$ ) of each DEB was 2000 mm, which was assumed to be sufficient since the extent of the D-region for both DEB<sub>B</sub> and DEB<sub>T</sub> was around 950 mm. The concrete blocks as supports had a length of 350 mm, a width of 175 mm and a height of 175 mm. The elements were discretized using a 0.1-m mesh size.

The elastic modulus of concrete,  $E_c$ , was taken as 27 GPa with a Poisson's ratio,  $\nu_c$  of 0.2. The CDP model inputs for the concrete tensile and compressive behavior is given in Figure 4c,d.<sup>51,59,69,70</sup> The dilation angle of the concrete was 31°, with an eccentricity of 0.1.<sup>59</sup> The elastic modulus of steel,  $E_s$ , was taken as 200 GPa with a Poisson's ratio,  $\nu_s$ , of 0.3 and a yield stress ( $f_{sy}$ ) of 450 MPa. The density of the concrete and the steel reinforcements were taken as 2400 and 7600 kg m<sup>-3</sup>, respectively. The steel reinforcements were embedded in the concrete using the embedded region feature, which is considered as a two-node linear three-dimensional truss. The concrete-to-concrete contact between DEB<sub>B</sub> and DEB<sub>T</sub> was defined by a penalty friction coefficient,  $\mu_{cc}$ , equal to 0.40. This is based on Wilden<sup>71</sup> where the concrete-to-concrete friction factor for dry condition is 0.80 and the prescribed safety factor of two. The contact analysis of the two DEBs was configured to not allow separation since there were no means for the DEB<sub>B</sub> and DEB<sub>T</sub> to remain intact.

An area load of 40 kN m<sup>-2</sup> was applied to a concrete cuboid (with a length of 175 mm, a width of 175 mm, and a height of 350 mm) at the critical location of the DEBs to account for the walls, roof loads, plasterboard partitions, flooring, and live loads (Figure 6a). Table 1 summarizes the input parameters for the numerical simulations with concrete block supports.

#### 3.1.2 | Soil-support simulations

The developed coupled hydro-mechanical model by Teodosio et al.<sup>51</sup> was used to conduct the numerical simulations of the DEB supported by reactive soils. This

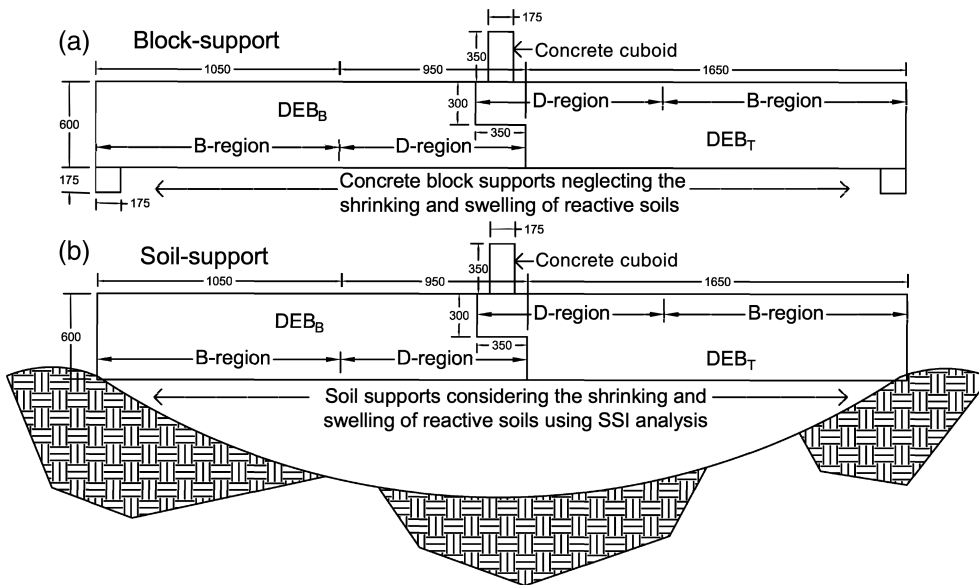


**FIGURE 6** Investigation of the effect of supports with (a) concrete block supports neglecting the presence and absence of soil pressure influencing the substructure, referred to as “block-support,” and (b) ground support considering the effect of the absence of soil contact (for shrinking scenario) and applied soil pressure (swelling scenario) due to reactive soil movements using the developed coupled hydromechanical model by Teodosio et al.,<sup>51</sup> referred to as “soil-support”

Notation	Parameter	Input values	References
$p$	Area load	40 kN m <sup>-2</sup>	[26]
$\rho_c$	Concrete density	2400 kg m <sup>-3</sup>	[51]
$E_c$	Elastic modulus of concrete	27 GPa	[59]
$\nu_c$	Poisson's ratio of concrete	0.2	[59]
$\mu_{cc}$	Friction coefficient (concrete-concrete)	0.40	[71]
$\rho_s$	Steel density	7600 kg m <sup>-3</sup>	[26]
$E_s$	Elastic modulus of steel	200 GPa	[72]
$\nu_s$	Poisson's ratio of steel	0.3	[28]
$f_{sy}$	Yield stress of steel	450	[72]
			[53]

**TABLE 1** Summary of input parameters for numerical simulations with concrete block-support

model considers SSI enabling the calculation of applied soil pressure onto footings and the investigation of change in  $C$  and  $T$  in the structural system. This set of simulations had identical configuration of dapped-end concrete beams and applied loads in the block-support simulations. The sole difference is the addition of a reactive soil mass underneath the substructure acting as a support.

To calculate the reactive soil movement influencing the displacement of footing systems, specific soil properties are required as inputs for Equation (1). The properties of the reactive soil mass used in the parametric simulations were based on the idealized Soil Water Characteristic Curve (SWCC) and the idealized moisture-swelling curve presented in Figure 3 by Shams et al.<sup>48</sup> The soil had a length of 8.0 m, a width of 3.0 m, and a height of 12.5 m, discretized using a 0.8-m mesh size adopted from the conducted boundary

conditions and mesh convergence analyses. The active depth zone ( $H_s$ ) was assumed to extend to 2.5 m from the ground surface, modeled as a reactive soil with moisture-swelling effect. Contrarily, the remaining soil layer from 3.0 to 12.5 m was modeled as a nonreactive soil without the moisture-swelling model. This reactive soil layer depth or  $H_s$  is based and within the prescribed typical values in the Standards Australia.<sup>29</sup> The elastic modulus of the soil,  $E_{soil}$ , was based on Standards Australia.<sup>29</sup> The value of  $E_{soil}$ , ranging from 1000 to 5000 kPa m<sup>-1</sup>, was dependent on the confining pressure of the soil and  $u$  (equal to  $\psi_w$ ).<sup>48</sup> The value of  $\nu_{soil}$  was assumed to be 0.3.<sup>48</sup> The density of the soil was assumed to be 1500 kg m<sup>-3</sup>. The permeability of the soil was assumed to be  $1 \times 10^{-6}$  cm s<sup>-1</sup>.

The initial parameters of the swelling reactive soil were  $-1.0 \times 10^4$  kPa for  $u$  and 0.3 for  $S$ , since the common initial condition in most sites are around these

values.<sup>73</sup> This assumption is based on a dry field that reached a stable value through equilibrium throughout the soil medium. The initial  $\sigma$  was calculated using the product of the initial  $u$  and the initial  $S$ , equal to  $-3.0 \times 10^3$  kPa applied uniformly throughout the soil medium. The initial value of void ratio ( $e$ ) was 1.2. The simulation for the swelling scenario had two steps, the first step was a static analysis performed to set-up the in-situ stresses and cancel out the soil deformation caused by the initial condition. The second step was a transient flow-deformation analysis where the final value of  $u$  in the uncovered ground was  $-6.0 \times 10^2$  kPa based on the average change in soil suction ( $\Delta\bar{u}$ ), stipulated in Standards Australia<sup>29</sup> equal to 1.2 pF. Stopping criteria of the developed coupled hydro-mechanical model for all simulations were based on Standards Australia.<sup>29</sup> A surface pore pressure ( $u$ ) or soil suction ( $u$ ) boundary condition was continuously applied to the open ground and was then terminated when a change at the bottom of the active depth zone,  $H_s$ , had occurred. Hence, the time required to complete each simulation run was 750,000 s.

The initial parameters of the shrinking reactive soil were  $-6.0 \times 10^2$  kPa for  $u$  and 80% for  $S$ , which was based on the final value of the swelling scenario and  $\Delta\bar{u}$  equal to 1.2 pF. In a wet field had reached a stable value through equilibrium, the initial  $u$  was assumed to be  $-6.0 \times 10^2$  kPa applied uniformly throughout the soil medium. The initial  $\sigma$  was calculated to be the product between the initial  $u$  and the initial  $S$  equal to  $-4.8 \times 10^2$  kPa applied uniformly throughout the soil medium. The initial value of  $e$  was 1.2. The simulation for the

shrinking scenario had two steps similar with the swelling scenario. The final value of  $\psi_w$  in the shrinking soil of the uncovered ground was of  $-1 \times 10^4$  kPa. Simulations were concluded when a change in  $u$  or  $\psi_w$  occurred right below  $H_s$ , similar with the swelling scenario.

The boundary condition at the outer edges of the reactive soil was restrained horizontally, only allowing vertical movements. The boundary conditions of the inner and outer surfaces of the nonreactive soil layer and the bottom of the soil mass were restrained against horizontal and vertical movements. The interaction between the substructure and reactive soil was defined by a soil to concrete friction contact using a penalty friction coefficient,  $\mu$ , equal to 0.35. On the other hand, the concrete to concrete interaction was assumed to have a  $\mu_{cc}$  equal to 0.40, similar with the block-support simulations. Tables 1 and 2 summarize the input parameters for the numerical simulations with swelling and shrinking soil supports.

### 3.2 | Simulation and optimization of the developed DEB and bolt connection

Simulations to investigate the potential strength of the developed connection designed using the combined SSI analysis,<sup>51</sup> TO and STM (Section 7 of Standards Australia<sup>65</sup>) were performed. The objectives of these simulations were, first, to validate the optimized steel reinforcement layout and, second, validate and optimize the connection details comprised of bolt diameter and bolt spacing at the discontinued portion.

**TABLE 2** Additional input parameters for numerical simulations with soil-support

Notation	Parameter	Input values	Reference
$\rho_b$	Soil bulk density	1500 kg m <sup>-3</sup>	[74]
$E_s$	Soil elastic modulus	1000–5000 kPa m <sup>-1</sup>	[48]
$\nu_{soil}$	Soil Poisson's ratio	0.3	[51] [48]
$\mu_{sc}$	Friction coefficient (soil-concrete)	0.35	[48] [51]
$k_{sat}$	Saturated permeability	$1 \times 10^{-7}$ ms <sup>-1</sup>	[74] [75]
$\psi_w$ versus $S$	Sorption curve or SWCC	Figure 3a	[74] [48]
$\epsilon_{ms}$ versus $S$	Moisture-swelling or shrink-swell curve	Figure 3b	[74] [76]
$\Delta\bar{u}$	Average suction change active depth zone	1.2 pF	[29]
$H_s$		2.5 m	[29]

### 3.2.1 | Validation and simulation considering the reinforcement layout

The peak load ( $V_u$ ) obtained in the laboratory test conducted by Mata-Falcón et al.<sup>53</sup> (specimen DEB 1.6) was compared to the simulated DEB using CDP model (Figure 4) with the same steel reinforcement layout and concrete dimensions with the experiment. This will validate the accuracy of the numerical simulations performed. The DEB from the experiment of Mata-Falcón et al.,<sup>53</sup> which was adopted in the simulation, had a span of 3300 mm and a rectangular cross-section of 250 mm by 600 mm, reduced to 250 mm by 300 mm at the end portion (i.e., D-region). Labels for each reinforcement is presented in Figure 7a, where  $A_{sf}$  is the flexural reinforcements,  $A_{st}$  is the shear reinforcement,  $A_{sh}$  is the horizontal bars at the D-region,  $A_{sv}$  is the vertical stirrups at the D-region, and  $A_{sd}$  is the diagonal stirrups at the D-region (Figure 7b). Steel reinforcements were 4–25  $\varnothing$  (1963 mm<sup>2</sup>) for  $A_{sf1}$ , 4–16  $\varnothing$  (804 mm<sup>2</sup>) for  $A_{sf2}$ , 4–8  $\varnothing$  at 125 mm spacing (1608 mm<sup>2</sup>) for  $A_{st}$ , 4–16  $\varnothing$  (804 mm<sup>2</sup>) for  $A_{sh}$ , 2–10  $\varnothing$  (157 mm<sup>2</sup>) for  $A_{sv1}$ , 2–12  $\varnothing$  (226 mm<sup>2</sup>) for  $A_{sv2}$ , and 2–10  $\varnothing$  (157 mm<sup>2</sup>) for  $A_{sv3}$ . This material layout (i.e., concrete for struts and steel reinforcement for ties) was designed using the European Committee for Standardization (CEN).<sup>78</sup>

The input parameters used for the material properties of concrete and steel are presented in Table 1. The CDP model inputs for the concrete tensile and compressive behavior with  $E_c$  of 27 GPa are given in Figure 4c,d.<sup>59</sup>

The simulated DEB specimen was simply-supported and then loaded using a three-point asymmetric bending set-up. The concentrated load was applied using a cylindrical rigid shell with a diameter of 100 mm to the center of the DEB, 1500 mm from the support at the reduced portion and 1000 mm from the other support (Figure 7a). The two supports were rigid shell elements with dimensions of 250 by 150 by 20 mm.

The developed DEB design had similar concrete section dimensions, material properties and simulation set-up with Mata-Falcón et al.<sup>53</sup> The only difference was the steel reinforcement layout shown in Figure 7b, designed using the combined SSI analysis, TO and STM. Steel reinforcements were 4–25  $\varnothing$  (1963 mm<sup>2</sup>) for  $A_{sf1}$ , 3–25  $\varnothing$  (1472 mm<sup>2</sup>) for  $A_{sf2}$ , 4–8  $\varnothing$  at 150 mm spacing (603 mm<sup>2</sup>) for  $A_{st}$ , 3–16  $\varnothing$  (603 mm<sup>2</sup>) for  $A_{sh}$ , 2–8  $\varnothing$  (101 mm<sup>2</sup>) for  $A_{sv1}$ , 2–8  $\varnothing$  (101 mm<sup>2</sup>) for  $A_{sd1}$ , 2–25  $\varnothing$  (982 mm<sup>2</sup>) for  $A_{sd2}$ , and 2–8  $\varnothing$  (101 mm<sup>2</sup>) for  $A_{sd3}$ . The developed DEB was simply-supported and loaded using the three-point nonsymmetric bending with material properties and load application similar with Mata-Falcón et al.<sup>53</sup> shown in (Figure 7).

### 3.2.2 | Validation and optimization of the bolt connection

Ultimate shear strength ( $V_u$ ) and ultimate moment capacity ( $M_u$ ) of a bolt connection from the experiment of Ousalem et al.<sup>72</sup> was used to investigate if comparable results will be obtained using numerical simulations. The

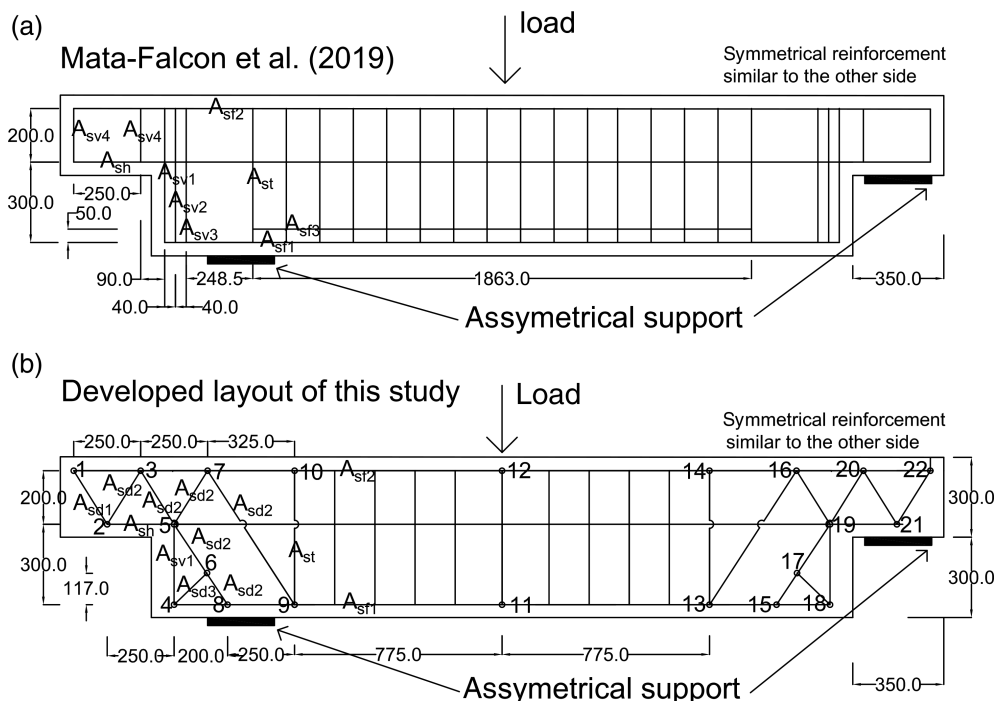


**FIGURE 7** Material layout and simulation setup of (a) the laboratory test (specimen DEB 1.6) by Mata-Falcón et al.<sup>53</sup> and Mata-Falcón,<sup>77</sup> and (b) the designed DEB of this study using the innovative combined approach of soil–structure interaction, topology optimization, and strut-and-tie model (STM). Dimensions are in millimeters. Figure 7b have numbered nodes for the STM calculations

dimensions of the DEB from the experiment and adopted in the simulation had a span of 3500 mm and a rectangular cross-section of 270 by 275 mm, reduced to 130 mm by 275 mm at the end portion (i.e., D-region). Steel reinforcements were 4–16  $\varnothing$  (804 mm<sup>2</sup>) as top flexural reinforcements, 4–16  $\varnothing$  (804 mm<sup>2</sup>) as bottom flexural reinforcements, and 4–6  $\varnothing$  spaced at 75 mm (113 mm<sup>2</sup> at 75 mm) as shear reinforcements reduced to 2–6  $\varnothing$  spaced at 75 mm (57 mm<sup>2</sup> at 75 mm) at the dapped-end portion. Eight M16 bolts were installed laterally at the dapped-end portion with 100 mm center-to-center spacing.

The elastic modulus of concrete,  $E_c$ , was taken as 38 GPa. The CDP model inputs for the concrete tensile and compressive behavior with  $E_c$  of 38 GPa are given in Figure 4c,d.<sup>59</sup> The remaining input parameters used for the material properties of concrete and steel are presented in Table 1.

The simulated DEB specimen by Ousalem et al.<sup>72</sup> was simply-supported and loaded using the four-point symmetric bending, similar to the laboratory testing. Concentrated load was applied using a 100-mm cylindrical rigid shell to the pure bending distance, 490 mm from the center of each side. The two supports were rigid shell elements with dimensions of 270 by 150 by 20 mm. The experimental set-up of the laboratory test conducted by Ousalem et al.<sup>72</sup> is presented in Figure 8a.

The developed DEB design presented in Figure 7b was simulated with varying bolt diameters (i.e., 12,

16, and 20 mm) and values of bolt spacing (i.e., 50, 150, and 250 mm) to determine the optimum configuration of the developed connection with acceptable  $V_u$  and  $M_u$ . The simulated developed DEB was simply-supported and loaded using (1) a four-point symmetric bending onto the connection with 700 mm distance between the loads for pure bending (Figure 8b) and (2) a three-point symmetric bending loaded onto the middle of the beam (Figure 8c). Geometry, steel reinforcement layout, and material properties were similar with the developed DEB in Figure 7b and Table 1.

### 3.3 | Behavior of the developed precast connection on reactive soils

A monolithic waffle pod raft and a prefabricated raft substructure, with the developed connection from the combined soil-substructure analysis, TO, and STM, were compared in both swelling scenario and shrinking scenario. The developed coupled hydro-mechanical model by Teodosio et al.<sup>51</sup> was used to conduct the numerical simulations supported by reactive soils. The finite element model only considered quarter of the entire soil mass and the raft substructure since the  $x$  and  $z$  axes were symmetrical.

The soil mass, where the monolithic waffle pod raft and the prefabricated raft substructure was constructed,

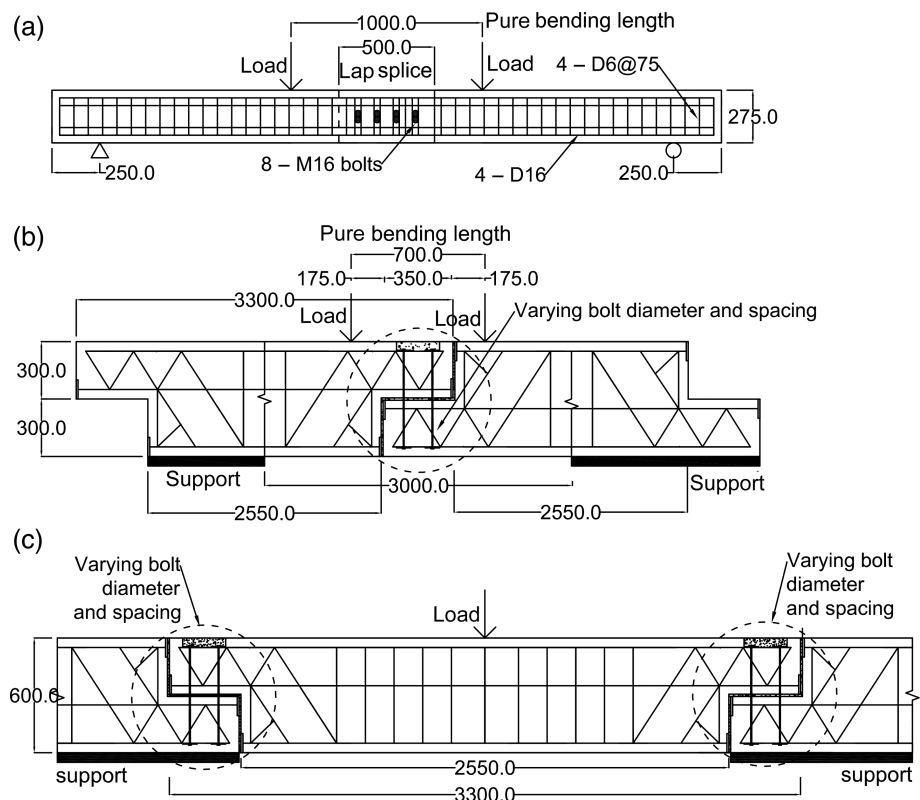


**FIGURE 8** Simulation of the developed DEBs showing (a) the four-point experimental set-up of Ousalem et al.<sup>72</sup> adopted for simulation, (b) the four-point bending simulation set-up with load applied near the connection of two jointed DEBs having a pure bending length of 700 mm, and (c) the three-point bending simulation set-up with load applied onto the mid-span of the middle DEB

was assumed to have an active depth zone,  $H_s$ , of 3.0 m. The length and width of the soil mass were assumed to be 30 m, while the depth of the soil mass was assumed to be 12.5 m. The input parameters used for the material properties of soil are presented in Table 2.

To determine the site classification described above, the soil mass was simulated without footings on top to calculate for the expected soil movement. The obtained expected soil movement ( $y_s$ ) was 85 mm. Hence, the site was classified as an extremely reactive (Class E).

The structural design details of the hypothetical monolithic waffle pod raft was determined by using Sections 4.5 and 4.6 of the AS 2870-2011.<sup>29</sup> In fig. 4.1 of the AS 2870-2011, the value of the vertical axis was 2.8, where  $y_s$  was 85 mm based on the performed simulation and  $\Delta_{\max}$  is the maximum allowable differential movement of the substructure equal to the lower value between  $L/400$  and 30 mm. Assuming a 16.1 by 16.1 m<sup>2</sup> floor area based on the average floor area (i.e., 230 m<sup>2</sup>) of single-detached dwellings in Australia,<sup>79</sup>  $\Delta_{\max}$  was taken as 30 mm. From the vertical axis, the value of  $y_s/\Delta_{\max}$  (i.e., 2.8) was projected to determine the unit stiffness ( $EI/L$ ) required for the monolithic waffle pod raft. The obtained unit stiffness value was 9.35 N/m. Using this value,  $D$  was calculated as

$$\frac{EI}{L} = \log \left[ \frac{\sum \frac{BD^3}{12}}{W} \right], \quad (7)$$

where  $W$  is the overall width of slab orthogonal to the  $L$  being considered. Assuming the monolithic waffle pod raft had  $B$  of 300 mm for the edge beams and 110 mm for the internal beams spaced at 1.2 m. The calculated depth of beams ( $D$ ) from Equation (7) was 610 mm with a slab thickness of 85 mm throughout the area. A total of 14 beams were present for each horizontal direction. Steel reinforcements were assumed to be 3–16 mm  $\varnothing$  (3 N16) for the edge beams, 1–16 mm  $\varnothing$  (1 N16) for the internal beams, and 8 mm  $\varnothing$  spaced at 200 mm (SL82) for the slab mesh. The input parameters used for the material properties of concrete and steel are presented in Table 2.

To effectively compare the two substructure systems, the calculated  $EI/L$  equal to 9.35 was used to determine the required  $B$ ,  $D$ , spacing of beams, and number of beams of the prefabricated substructure assuming the length, width, and area of the prefabricated system was similar to the hypothetical monolithic waffle pod raft (16.1 by 16.1 m<sup>2</sup>). From the calculation, the prefabricated raft was designed to have a  $B$  of 250 mm for the edge beams and internal beams,  $D$  of 600 mm and beam spacing of 2.3 m. The values of  $B$  and  $D$  were similar with the

developed DEB in Figures 7b and 8b,c. The prefabricated raft substructure should have eight beams to have an equivalent unit stiffness with the monolithic waffle pod raft. Steel reinforcements were similar to Figure 7b with bolt connections as specified in the results of Figure 8b,c. Slab thickness was taken as 85 mm throughout the area. The value of  $p$  was 2500 kN m<sup>-2</sup> and the value of  $q$  was 6500 m<sup>-1</sup>. The material properties (i.e., concrete and steel) of the developed DEB was similar to the previous simulations, presented in Figure 4c,d with  $E_c$  equal to 27 GPa.

The developed prefabricated was sliced into 28 panels. Since the finite element simulations only considered quarter of the entire soil mass and the raft substructure due to the  $x$  and  $z$  axes symmetry, only quarter of the sliced prefabricated substructure was considered (Figure 9a). The monolithic waffle pod raft with similar  $EI/L$  with the prefabricated footing is shown in Figure 9b.

## 4 | RESULTS AND DISCUSSION

Important observations are highlighted in this section for the developed prefabricated connection using the proposed combined approach of SSI analysis, TO, and STM. First, the difference in  $C$  and  $T$  between neglecting the soil pressure due to shrink-swell ground movements and considering the effect of soil pressure induced by reactive soil is presented. Second, the similarity of resulting STMs from the physical-based SSI analysis and the stochastic TO is discussed. Third, the validation, simulation, and optimization of the developed connection for prefabricated raft footings using the combined approach. Last, the comparison of the soil-structure behavior between a monolithic waffle pod raft and a prefabricated raft substructure utilizing the developed connection through numerical simulations.

### 4.1 | Comparison between block-support and soil-support simulations

A comparison between an approach neglecting the soil pressure due to shrink-swell ground movements, termed as block-support in this study, and an approach considering the effect of soil pressure induced by reactive soil movements, termed as soil-support, was performed.

$C$  and  $T$  with load applications onto the critical location are presented for both block-support and soil-support in Figure 10. The results showed that  $C$  and  $T$  experienced by a connected substructure with soil-support obtained higher magnitude of stresses on

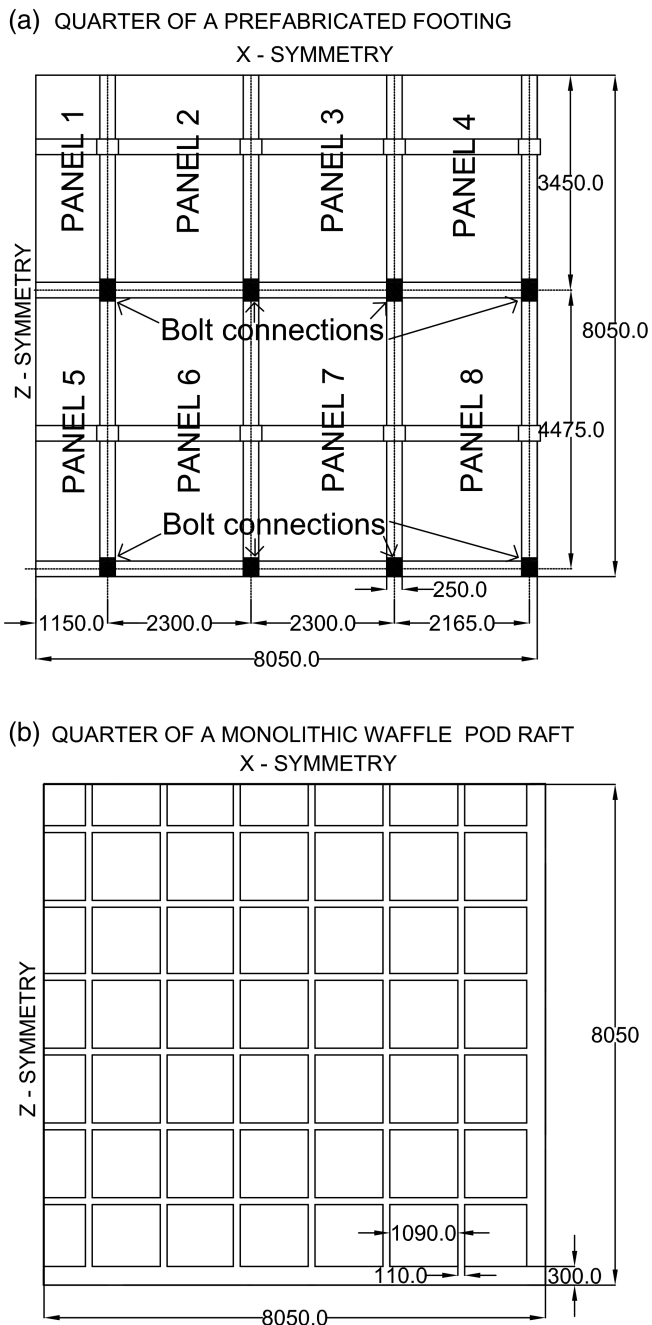


**FIGURE 9** Plan view of (a) quarter of the developed prefabricated raft footing ( $16.1$  by  $16.1$  m<sup>2</sup>) with panelized intergrated slab and beams, and (b) quarter of the monolithic waffle pod raft for comparison. The designed connection using the developed approach combining soil–structure interaction, topology optimization, and strut-and-tie model was used (Figure 1). Dimensions are in millimeter and not drawn to scale

swelling soil (Figure 10).  $C$  developed in the dapped-end portion of the prefabricated substructure with a simply-supported configuration started from the loading block propagating to the reduced portion and the upper part of the beam (Figure 10a). Contrarily, the connected footings with soil-support due to swelling soil had an additional

compressive load applied underneath the bottom ends acting as supports and adding pressure, leading to a lenticular space in the middle where the beam acted as simply-supported (Figure 10b). Due to this, the development of STMs will differ between the obtained geometry obtained using the block-support and the soil-support simulations. An approximate compressive flows for both simulations were drawn using white lines, giving relatively different strut-and-tie geometry. Similarly,  $T$  for the block-support was concentrated in the connection of the dapped-end portions (Figure 10c), while swelling soil added tension at the bottom and upper parts of both connected beams (Figure 10d).

For the DEBs experiencing negative bending due to shrinking soil (Figure 11),  $C$  and  $T$  resulted from simulations with block-support and soil-support were comparable. From the results of the soil-support simulations, it can be observed that for footings on shrinking soil with longer span,  $C$  and  $T$  are relatively lesser than that of simulations with block-support regardless of the location of connections and load application. This is due to the soil acting as a flexible support providing more uniform contact with footings when span of the substructure is longer.

The comparison of footings with soil-support on swelling soil obtained higher  $C$  and  $T$  than simulations with block-support, due to the additional pressure provided by the contact between reactive soil and concrete beams. On the other hand, footings with soil-support on shrinking soil had comparable  $C$  and  $T$  with that of block-support simulations. Moreover,  $C$  and  $T$  were reduced when the span of the substructure is longer due to a more uniform and flexible support of the ground rather than a rigid block support.

## 4.2 | Comparison of the STMs using SSI analysis and TO

The similarity of the developed STMs from the physical-based SSI analysis and the stochastic TO is discussed in this section.

Combining  $C$  and  $T$  in Figures 10 and 11, the STM developed using the SSI analysis is shown in Figure 12a. The optimum STMs using TO for the bottom DEB and the top DEB are shown in Figure 12b,c, respectively. The developed STMs of the SSI simulations and TO were comparable. Both models formed a triangular truss-like configuration for both bottom DEB (i.e., void at the top) and top DEB (i.e., void at the bottom). In the TO approach, the configuration of the bottom DEB was similar with the top-dapped end beam. However, additional lines were laid out in the bottom DEB, at the

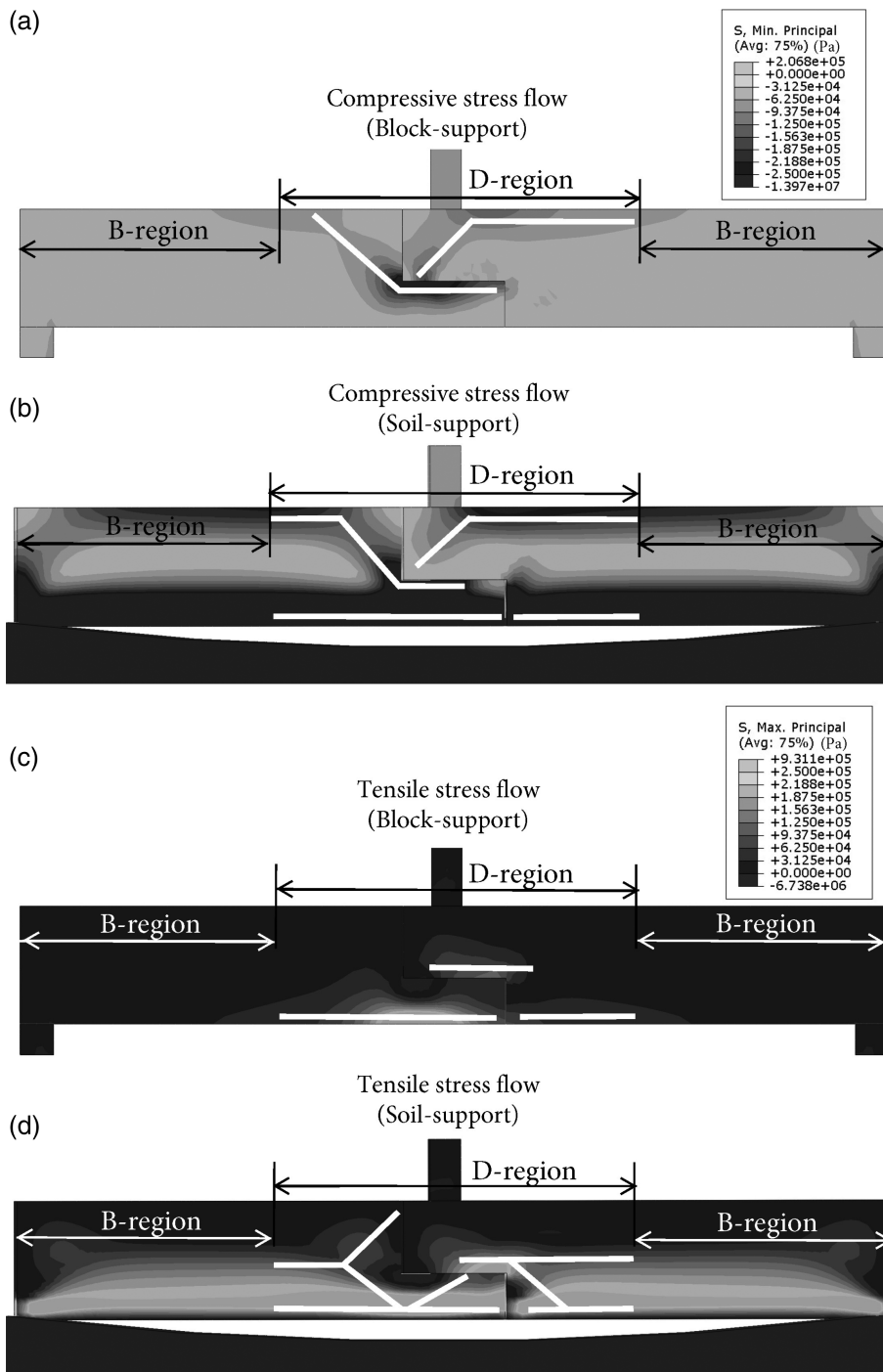


**FIGURE 10** Compressive stress flow ( $C$ ) in footings with an applied concentrated load onto the middle, showing (a) block-support and (b) soil-support on swelling soil. Tensile stress flow ( $T$ ) in footings with an applied concentrated load onto the middle, showing (c) block-support and (d) soil-support on swelling soil

intersection of the full portion and the reduced portion (i.e., re-entrant corner) termed as hanger reinforcements (Figure 12b). Hanger reinforcements were similar with the STM developed from the SSI analysis (Figure 12a). These hanger reinforcements are necessary to have sufficient counteracting force against the diagonal  $T$  due to the applied load onto the reduced part, in Figure 10d, causing failure due to the diagonal tension emanating from the re-entrant corner.<sup>71</sup>

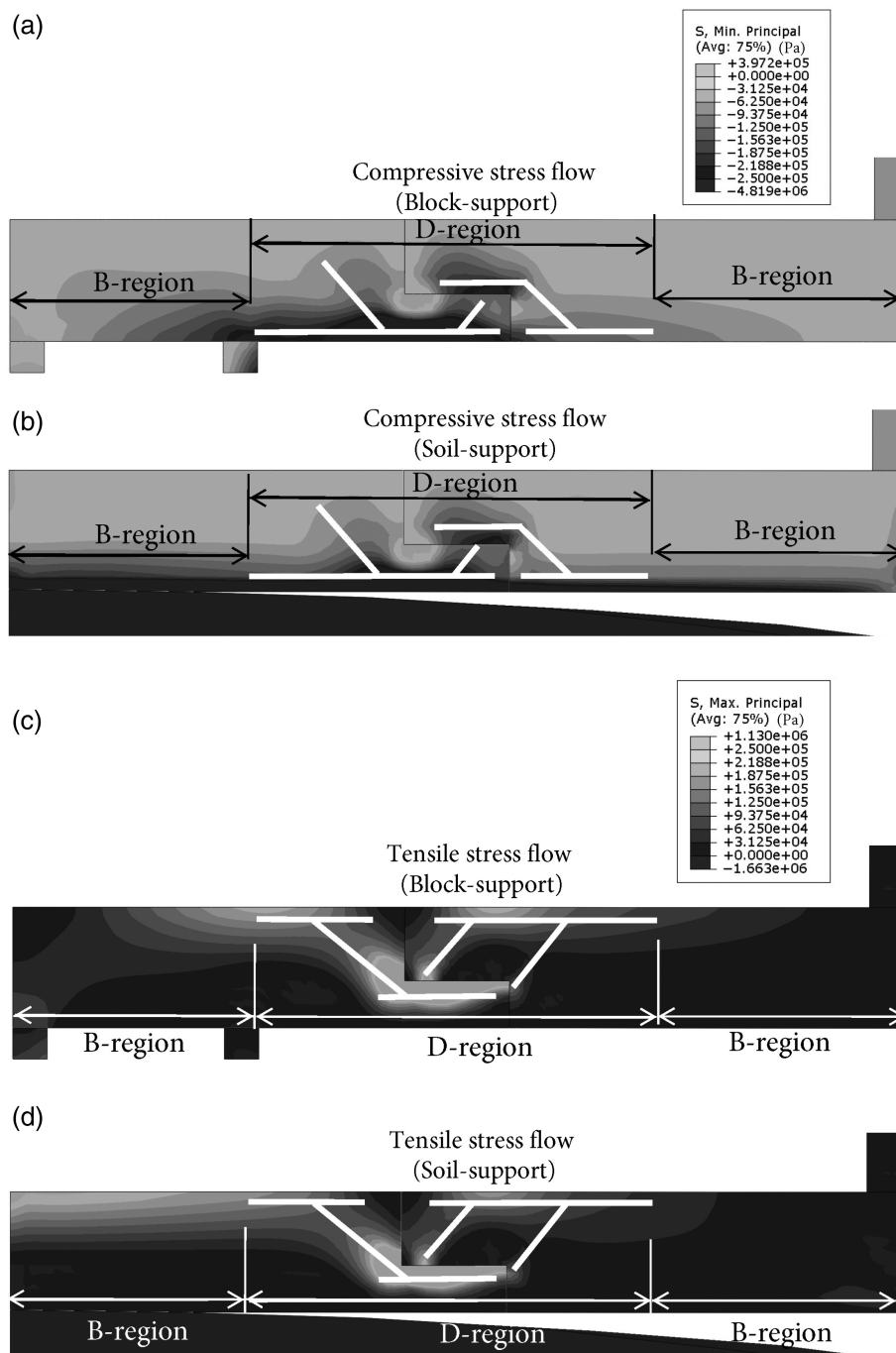
The obtained STMs from the physical-based SSI analysis and the stochastic TO were comparable. Thus, the

adopted STM to develop a prefabricated connection for substructure was similar to the findings in this section, shown in Figure 7b.

### 4.3 | Developed bolt connection

The potential ultimate strength of the designed connection using the developed approach combining SSI analysis,<sup>51</sup> TO, and STM, was determined through, first, by validating and simulating the optimized steel

**FIGURE 11** Compressive stress flow ( $C$ ) in footings with an applied concentrated load onto the edge, showing (a) block-support and (b) soil-support on shrinking soil. Tensile stress flow ( $T$ ) in footings with an applied concentrated load onto the edge, showing (c) block-support and (d) soil-support on shrinking soil



reinforcement layout and, second, by validating and optimizing the connection details, with consideration of the bolt diameter and the bolt spacing at the discontinued portion (Objectives 1 and 2 in Figure 1). The results and discussion are presented in the following sections.

#### 4.3.1 | Validation and simulation considering reinforcement layout

The laboratory test conducted by Mata-Falc3n et al.<sup>53</sup> was used to validate the peak load ( $V_u$ ) of the DEB

simulations. The DEB specimen had an asymmetric three-point configuration laboratory test set-up (Figure 7a), which was simply-supported and then loaded using a rigid cylinder onto the mid-span. The obtained simulated  $V_u$  of the DEB was equal to 306 kN (Figure 13a). The simulated value of  $V_u$  was comparable to the laboratory test results of Mata-Falc3n et al.,<sup>53</sup> equivalent to 309 kN (i.e., Specimen DEB 1.6), with a percentage difference of 1%. The first yielding of the DEB for the laboratory test was 63% of  $V_u$  and for the simulation was 65% of  $V_u$ . The slight difference between the simulated and experimental force-displacement curves may be

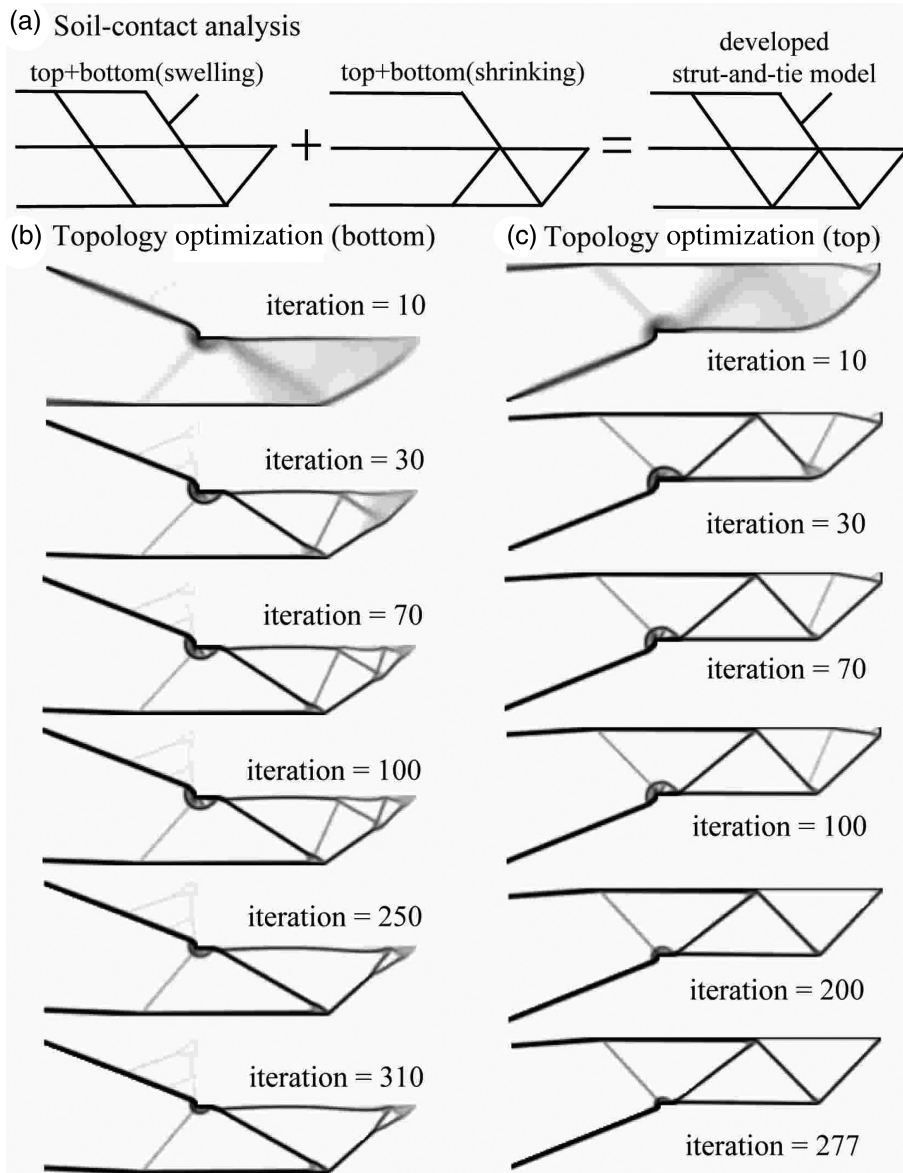


FIGURE 12 Obtained strut-and-tie models from (a) the soil–structure interaction numerical simulations with combined  $C$  and  $T$  (Figures 10 and 11), and (b) the topology optimization (TO) of the bottom DEB of the prefabricated substructure and (c) the TO of the top DEB of the prefabricated substructure

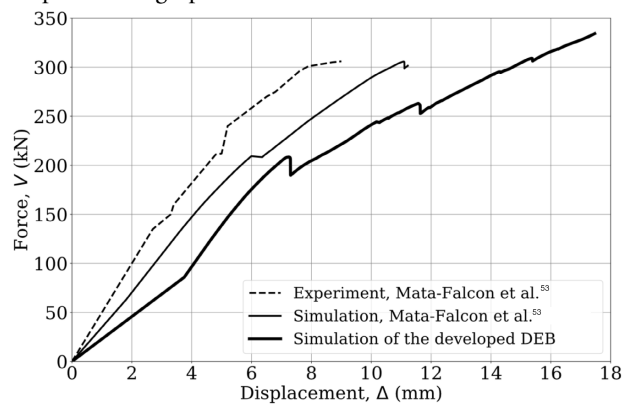
due to the aggregated factors of human error and experimental error during the laboratory testing or parameters that were used in the simulations since the CDP inputs were obtained from a different source by Hafezolghorani et al.<sup>59</sup> The spalling of the concrete cover in the laboratory test was not thoroughly captured in the simulation. However, the simulated cracking of concrete reflected the laboratory test results of Mata-Falcón et al.,<sup>53</sup> shown in Figure 13b. The simulated cracking started from the re-entrant corner and propagated upward through the hanger reinforcements, where majority of the cracking and damage occurred. The results of the comparison between the experimental test of and the simulated DEB of Mata-Falcón et al.<sup>53</sup> gives confidence on the succeeding finite element analyses for the developed DEB with optimum material layout. This validated the accuracy and applicability of the simulation set-up and

input parameters for concrete (i.e., CDP parameters) and steel.

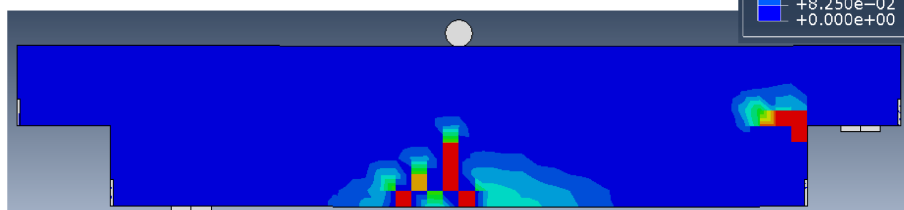
The developed DEB design, using the combined SSI, TO, and STM, had similar concrete section dimensions and simulation set-up adopted from Mata-Falcón et al.<sup>53</sup> The only difference was the steel reinforcement layout shown in Figure 7b. The DEB specimen also had an asymmetric configuration laboratory test set-up, with progressive load application until  $V_u$  was reached. The obtained  $V_u$  of the developed design 334 kN (Figure 13a). The peak load,  $V_u$ , was experienced in a higher value of displacement,  $\Delta$ , than that of the simulated DEB based on Mata-Falcón et al.<sup>53</sup> The first yielding of the simulated developed DEB was 31% of  $V_u$ , which was much lower than the simulated DEB adopted from Mata-Falcón et al.<sup>53</sup> (equal to 65%). This reflected that the developed DEB exhibited a more ductile behavior than that of

**FIGURE 13** Simulated cracking damage of (a) the laboratory test (specimen DEB 1.6) by Mata-Falcón et al.<sup>53</sup> and Mata-Falcón,<sup>77</sup> and (b) the DEB developed using the combined approach of soil–structure interaction, topology optimization, and strut-and-tie model. Concrete cracking occurred when the value of DAMAGET ( $d_t$ ) was greater than zero. Typical concrete damage is classified as (1) hairline cracks ( $\text{DAMAGET}(d_t) < 0.25$ ), (2) fine but noticeable cracks ( $0.25 \leq \text{DAMAGET}(d_t) < 0.85$ ), (3) distinct cracks ( $0.85 \leq \text{DAMAGET}(d_t) < 0.99$ ), and (4) wide cracks or gaps ( $\text{DAMAGET}(d_t) \geq 0.99$ ) based on the appendix C of Standards Australia<sup>29</sup>

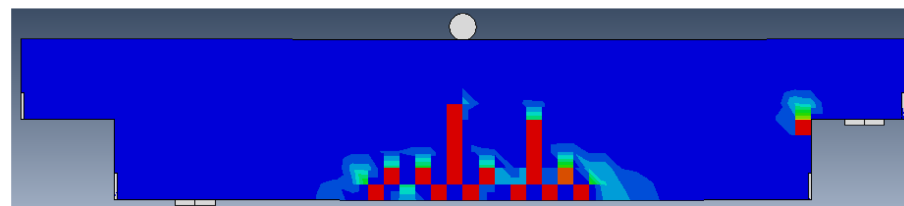
(a) Force–displacement graphs



(b) Simulated dapped-end beam based on the experiment of Mata-Falcon et al. (2019)



(c) Simulated dapped-end beam of this study



Mata-Falcón et al.<sup>53</sup> The simulated concrete cracking propagation of the developed DEB was similar with that of the simulated cracking of Mata-Falcón et al.<sup>53</sup> (Figure 13c). The majority of the damage and cracking occurred around the hanger reinforcements at the re-entrant corner. However, the propagation was relatively more concentrated in the said area lower than the top flexural steel reinforcements. Furthermore, the propagated cracking in the B-region of the developed DEB extended further upward compared to Mata-Falcón et al.<sup>53</sup> due to lesser reinforcements for the tensile portion and greater spacing of ties. The steel reinforcement required for the developed DEB was 15% lesser than the design of Mata-Falcón et al.<sup>53</sup> (i.e., specimen DEB 1.6). This is acceptable since the strain distribution in the B-region is linear.

The simulated  $V_u$  of the developed DEB with material layout based on the proposed combined method provided higher  $V_u$  and exhibited a more ductile behavior than the design of Mata-Falcón et al.<sup>53</sup> Thus, obtaining an

optimum material layout based on the developed approach combining SSI, TO, and STM is advantageous to design a beam-to-beam connection.

#### 4.3.2 | Validation and optimization of the bolt connection

The validation of a bolt connection was simulated through the laboratory experiment performed by Ousalem et al.<sup>72</sup> shown in Figure 8a. The DEB test specimen was simply-supported and loaded using the four-point symmetric bending set-up, which was adopted in the simulation. The simulated  $V_u$  and  $M_u$  were 76 kN and 76 kN m, which is commensurable with the laboratory test equal to 74 kN and 74 kN m, respectively. This validated the accuracy and applicability of the simulation set-up and input parameters for concrete, steel, and bolts used in the finite element analyses.

The developed DEB design, presented in Figures 7b and 13c, was used and connected using varying bolt diameters (i.e., 12, 16, and 20 mm) and values of bolt spacing (i.e., 50, 150, and 250 mm) to determine the optimum configuration of the developed connection. The configuration of the simulations (1) had a four-point symmetric bending set-up loaded onto the connection (Figure 8b) and (2) had a three-point symmetric bending set-up loaded onto the middle of the beam (Figure 8c).

Results of the simulated four-point symmetric bending set-up loaded onto the connection (Figure 14) obtained values of  $V_u$  ranging from 335 to 431 kN. The highest simulated values of  $V_u$  were from the monolithic beam and the

DEBs with 20-mm bolts and 150-mm spacing. Contrarily, the lowest simulated value of  $V_u$  was from the DEBs without the bolt connection. This is similar with the obtained values of  $M_u$ , where the highest simulated values were from the monolithic beam and the DEBs with 20-mm bolts and 150-mm spacing (54 kN m) and the lowest simulated value of  $M_u$  was from the DEBs without bolt connection (42 kN m). From the load–displacement graphs in Figure 14, it can be observed that the beam capacity is not governed by the connection but by shear failure of DEBs since the values of  $V_u$  are comparable to the monolithic beam. Thus, applying the load on to the connection shows that the connection is not the critical part.

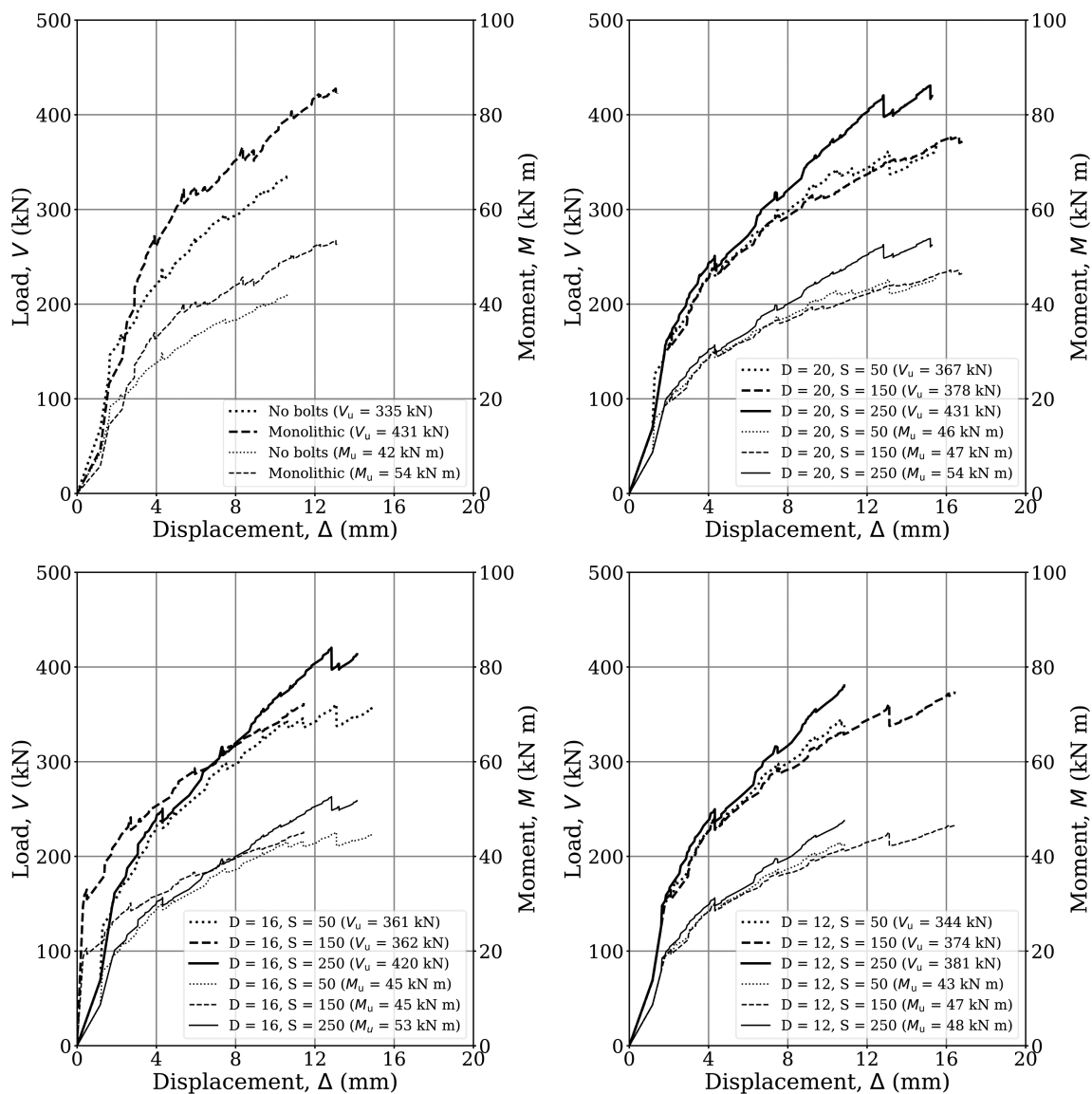


**FIGURE 14** Results ( $V_u$ ) of the four-point symmetric bending simulations loaded onto the connection with (a) monolithic beam and DEBs without the bolt connection, (b) DEBs with 20-mm bolt connectors with varying spacing (i.e., 50, 150, and 250 mm), (c) DEBs with 16-mm bolt connectors with varying spacing (i.e., 50, 150, and 250 mm), and (d) DEBs with 12-mm bolt connectors with varying spacing (i.e., 50, 150, and 250 mm)

Results of the simulated three-point symmetric bending set-up loaded onto the mid-span of the middle DEB (Figure 15) obtained values of  $V_u$  ranging from 205 to 419 kN. The highest simulated value of  $V_u$  was from the monolithic beam equal to 419 kN. On the other hand, the lowest simulated value of  $V_u$  was 205 kN from the DEBs without the bolt connection that is less than half of the monolithic beam. Similarly, the obtained highest simulated value of  $M_u$  was from the monolithic beam (70 kN m) and the lowest simulated value of  $M_u$  was from the DEBs without bolt connection (26 kN m). This is 37% of the  $M_u$  of the monolithic beam. The simulations with load applied on to the mid-span show that the configuration of the bolt connection affected the shear flow. Thus, connected DEBs can fail in shear or combined

shear and flexure. The nearest values of  $V_u$  and  $M_u$  to that of the monolithic beam was the bolt connection with 20-mm diameter and 150 mm spacing equal to 375 kN and 47 kN m (89% and 47% of the monolithic beam). This configuration was adopted in the SSI analysis to investigate the behavior of the prefabricated substructure with the developed bolt connection, shown in Figure 16.

#### 4.4 | Behavior of the prefabricated substructure with the developed bolt connection

The structural behavior of the prefabricated raft substructure on reactive soil, with the developed connection from

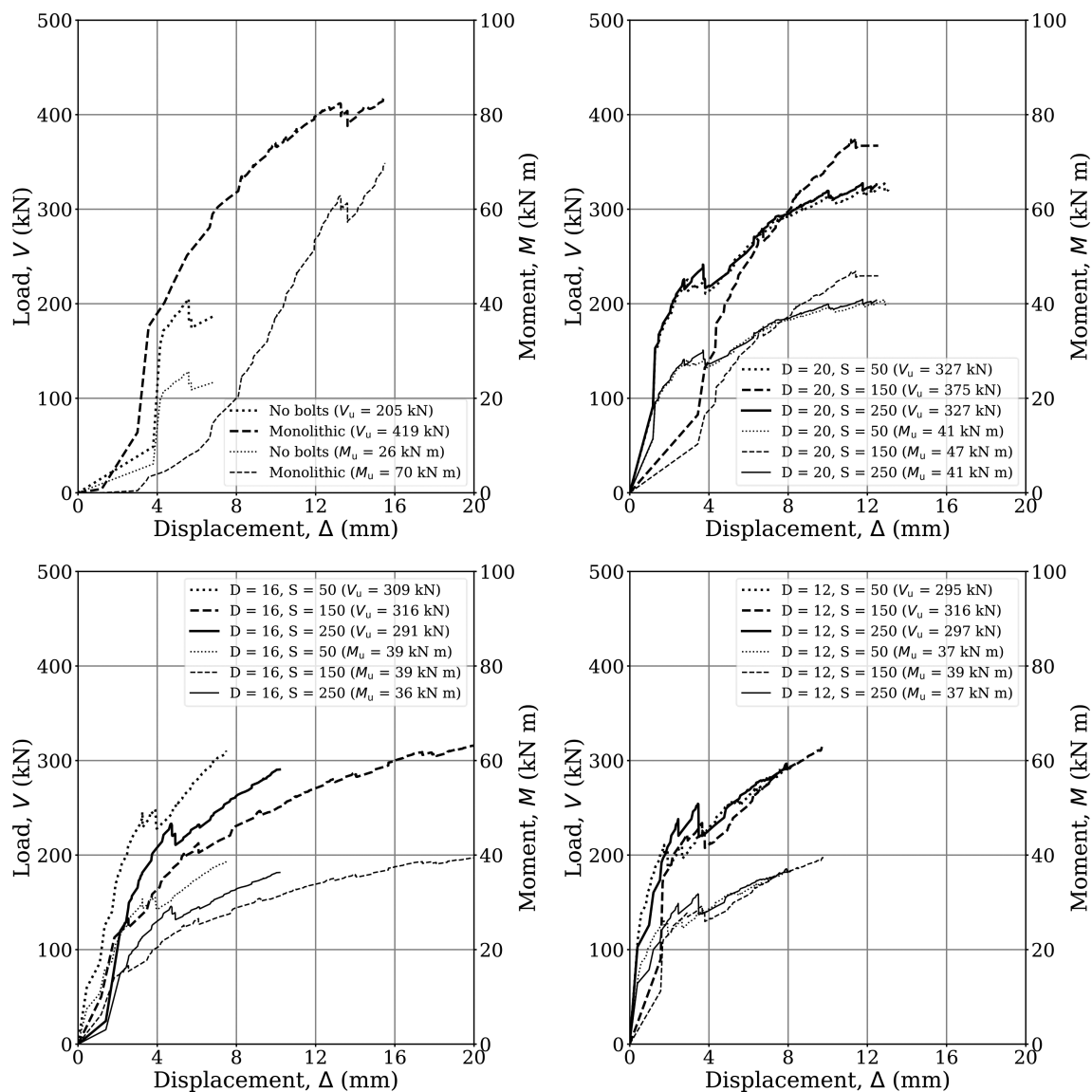
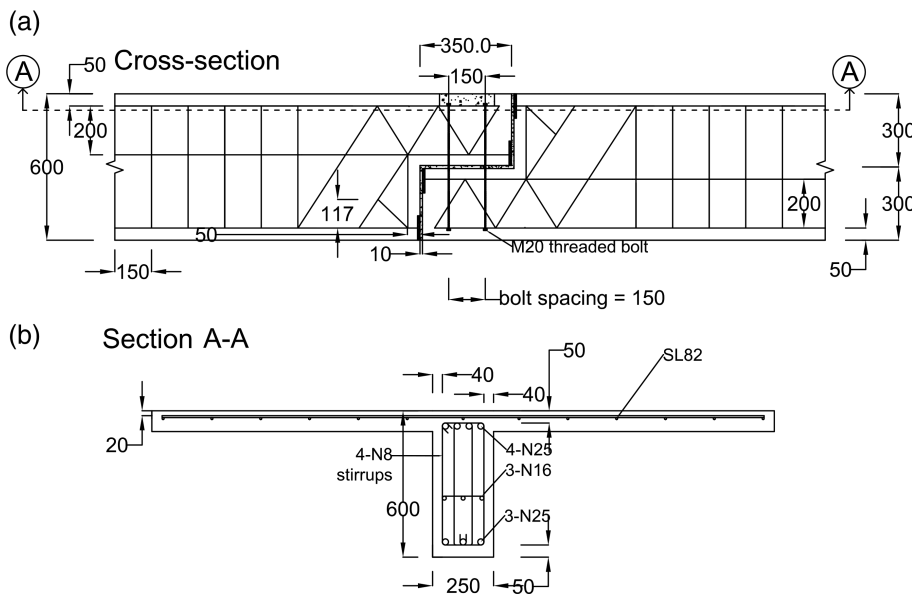
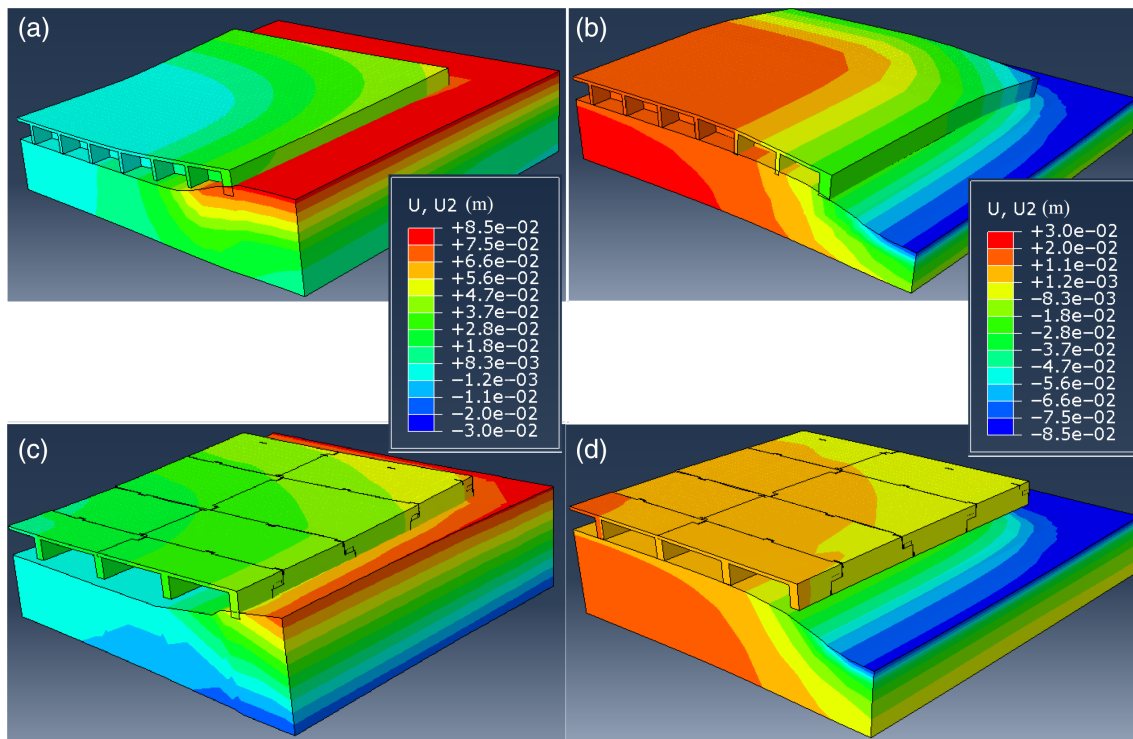


FIGURE 15 Results ( $V_u$ ) of the four-point symmetric bending simulations loaded onto the connection with (a) monolithic beam and DEBs without the bolt connection, (b) DEBs with 20-mm bolt connectors with varying spacing (i.e., 50, 150, and 250 mm), (c) DEBs with 16-mm bolt connectors with varying spacing (i.e., 50, 150, and 250 mm), and (d) DEBs with 12-mm bolt connectors with varying spacing (i.e., 50, 150, and 250 mm)



**FIGURE 16** Developed DEB with bolt connection used in Figure 9, using soil–structure interaction, topology optimization, and strut-and-tie model, showing (a) the cross-section and (b) Section A-A. Dimensions are in millimeter and not drawn to scale



**FIGURE 17** Soil–structure interaction showing movements between (a) the monolithic waffle pod raft and swelling reactive soil, and (b) the monolithic waffle pod raft and shrinking reactive soil. soil–structure interaction showing movements between (c) the prefabricated substructure, with the developed connection, and swelling reactive soil, and (d) the prefabricated substructure, with the developed connection, and shrinking reactive soil. The soil movements and substructure deformations are in meter

the combined soil-substructure analysis, TO and STM (Figure 16), was compared with a monolithic cast-in-place waffle pod raft. The hypothetical monolithic waffle pod raft was assumed to have 16.1 by 16.1 m<sup>2</sup> floor area based on the average floor area (i.e., 230 m<sup>2</sup>) of single-detached dwellings in Australia.<sup>79</sup>

The developed bolt connection was installed as specified in Figure 9. Details of the developed connection is shown in Figure 16.

The simulated shrink-swell soil movements and substructure deformations are presented in Figure 17 and Table 3. The prefabricated substructure with the

developed connection had generally lower deformation induced by the swelling soil and shrinking soil. The monolithic waffle pod raft had exceeded the acceptable

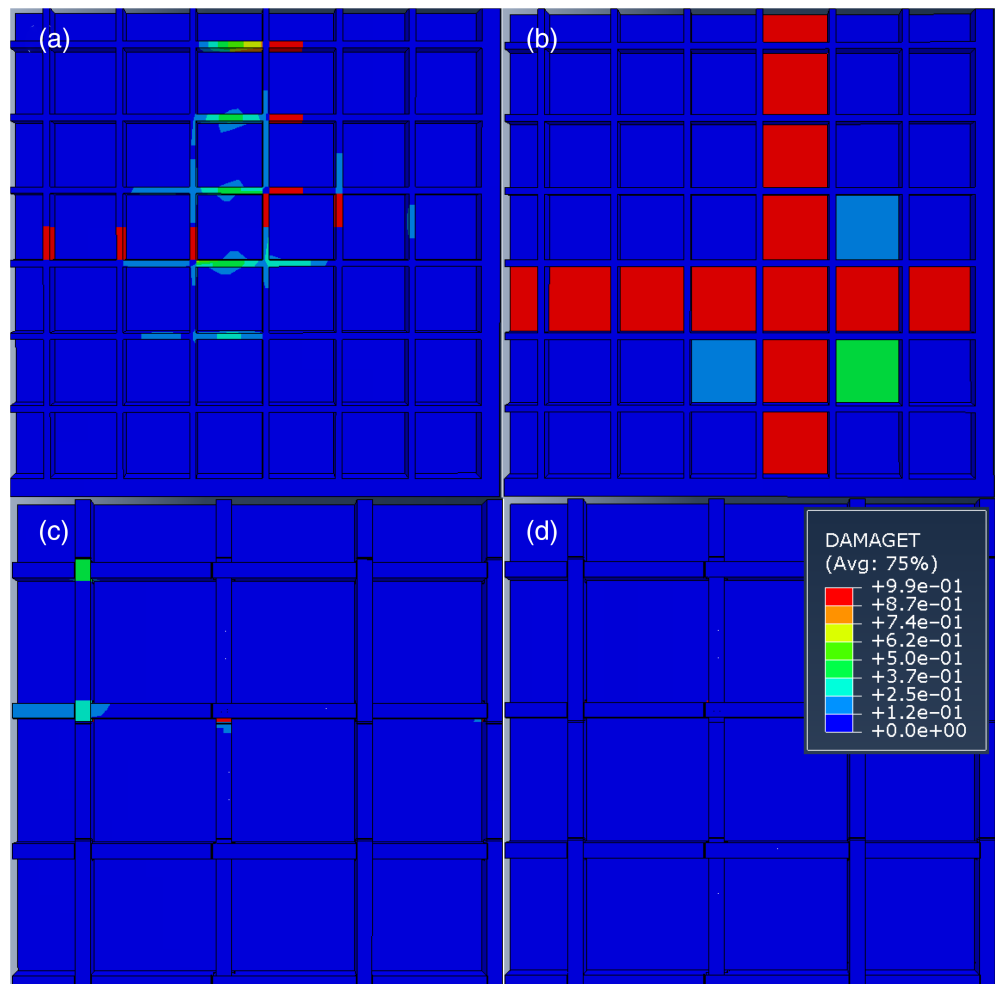
**TABLE 3** Simulated shrink-swell soil movements and substructure deformations of the monolithic waffle pod raft and the prefabricated raft substructure with the developed connection

	Substructure deformation, $\Delta$ (mm)	Differential soil movement, $y_m$ (mm)	Soil movement, $y_s$ (mm)
Monolithic waffle (swelling)	55	65	85
Monolithic waffle (shrinking)	72	78	85
Prefabricated raft (swelling)	40	60	88
Prefabricated raft (shrinking)	19	75	82

structural deformation for both swelling and shrinking scenarios. On the other hand, the prefabricated substructure had significant reduction of structural deformation due to the steel reinforcement layout designed for both positive and negative bending moment to consider the swelling and shrinking of reactive soil. The monolithic waffle pod raft deformed excessively, particularly on shrinking soil, because the reinforcing steel bar was only located at the bottom part as stipulated in AS 2870-2011. This design does not consider the behavior of monolithic pod raft on shrinking reactive soil inducing negative moment to the system. The simulated deformation of both footings had exceeded the serviceability limit state (SLS), which can be caused by, first, an underestimated value of  $EI/L$  from AS 2870-2011, second, consideration of nonlinear material behavior and plastic failure mechanisms, and last, captured effect of coupled three-dimensional hydro-mechanical analysis showing the critical values at the re-entrant corners (Figure 17) that cannot be considered in two-dimensional analysis.

Comparison of structural cracking of concrete, with  $d_t > 0$ , between the investigated raft footings (i.e., monolithic waffle pod raft and prefabricated

**FIGURE 18** Comparison of experienced cracking between the monolithic waffle pod raft and the prefabricated substructure with the developed connection (refer to Figure 9). DAMAGET ( $d_t$ ) greater than zero reflects cracking in (a) the monolithic waffle pod raft on swelling soil, (b) the monolithic waffle pod raft shrinking soil, (c) the prefabricated substructure on swelling soil, and (d) the prefabricated substructure on shrinking soil. Typical concrete damage is classified as (1) hairline cracks ( $\text{DAMAGET } (d_t) < 0.25$ ), (2) fine but noticeable cracks ( $0.25 \leq \text{DAMAGET } (d_t) < 0.85$ ), (3) distinct cracks ( $0.85 \leq \text{DAMAGET } (d_t) < 0.99$ ), and (4) wide cracks or gaps ( $\text{DAMAGET } (d_t) \geq 0.99$ ) based on the appendix C of Standards Australia<sup>29</sup>



substructure) and reactive soils is shown in Figure 18. The monolithic waffle pod raft had extensive structural cracking for both swelling scenario (Figure 18a) and shrinking scenario (Figure 18b). The bottom of the monolithic waffle pod raft is shown in Figure 18a, where the cracking damage were mainly experienced at the third to the fifth rows and columns from the center. The top view of the monolithic waffle pod raft is shown in Figure 18b. The rupture started from the re-entrant corner and propagating extensively through the beams and slabs. Contrarily, the prefabricated substructure with the developed connection had minimal structural damage at the bolt connections (Figure 18c,d).

The prefabricated substructure with the developed connection had generally lower deformation and lesser structural damage induced by the swelling soil and shrinking soils. This is attributed to the steel reinforcement layout designed using the combined approach of SSI analysis, TO, and strut-and-tie method. Thus, making the prefabricated raft substructure ideal for both positive and negative bending moments caused by the swelling and shrinking of reactive soils. The prefabricated system was governed by the SLS but not the ultimate limit state (ULS), with maximum steel reinforcement stress of less than 350 MPa. Contrarily, the monolithic waffle pod raft was governed by both ULS and SLS with a maximum structural deformation greater than 30 mm and steel reinforcement stress of both beams and slab greater than 450 MPa at the area where concrete cracking occurred for both shrinking and swelling soil scenarios.

## 5 | CONCLUSION

Developing the connection for prefabricated raft footings on reactive soil using the combined approach of SSI, TO, and STM had specific advantages in designing a more robust structural system. First, considering the effect of the existence (i.e., contact) or absence (i.e., separation) of pressure exerted by the soil changes the simulated compressive and tensile flow experienced by the structure. Second, the obtained STMs from the physical-based SSI analysis and the stochastic TO were comparable, giving confidence to the overall DEB and bolt connection design. Last, the simulated prefabricated substructure with the developed connection had higher ultimate strength and reduced simulated structural deformation and cracking due to the material layout (i.e., concrete as struts and steel as ties) designed for both positive and negative bending moment considering the swelling and shrinking of reactive soils. This design can be suitable for residential structures, mass housing, educational institutions, emergency structures, and postdisaster

reconstruction constructed on reactive soils. Further test verification and consideration of modular coordination, handling and transportation, and assembly are required. The developed prefabricated footing complies with the stipulations in AS 2870-2011, which is applicable to light-weight structures on reactive soils. However, further simulations are needed to specify required unit stiffness, reinforcement, and concrete sections depending on site classification (i.e., Class M, H<sub>1</sub>, or H<sub>2</sub>).

## ACKNOWLEDGMENT

The authors would like to thank the Australian Research Council—Centre for Advanced Manufacturing of Prefabricated Housing (ARC-CAMP.H), Industrial Transformation Training Centres—Grant ID: IC150100023 (2015–2018).

## DATA AVAILABILITY STATEMENT

The data that support the findings of this study are available from the corresponding author upon reasonable request.

## ORCID

Bertrand Teodosio  <https://orcid.org/0000-0002-3909-4054>

Kasun Shanaka Kristombu Baduge  <https://orcid.org/0000-0001-5183-701X>

## NOMENCLATURE

$\epsilon_T, \epsilon$	total and soil strain
$\epsilon_{es}, \epsilon_{ms}$	soil effective, swelling strain
$k_{sat}, k_u$	saturated/unsaturated permeability
$\psi_w, u$	soil suction, pore water pressure
$h, t$	water potential head, time
$m_{sw}$	slope of the sorption curve
$\gamma_w$	unit weight of water
$f_{k_u}$	permeability factor
$S, Q$	soil saturation, water flux
$\omega, \theta$	gravimetric/volumetric soil moisture
$\theta_r, \theta_s$	residual/saturated $\theta$
$\alpha, n, m$	empirical sorption curve parameters
$\rho_w, \rho_b$	water and soil bulk density
$e_0, e$	initial and instantaneous void ratio
$G_s, g$	specific gravity of solids, acceleration
$\sigma, \sigma'$	total and effective stress
$E, E_{soil}$	soil elastic constants, soil modulus
$G, \nu_{soil}$	shear modulus, soil Poisson's ratio
$\nu_c, \nu_s$	Poisson's ratio of concrete, steel
$\sigma_{dev}$	deviatoric stress
$\sigma_{t0}, \sigma_c$	tensile, compressive failure stress
$\sigma_t, \sigma_c$	tensile, compressive concrete stress
$\sigma_{cu}$	ultimate compressive concrete stress
$\epsilon_t, \epsilon_c$	tensile, compressive concrete strain

DEB	dapped-end beam
STM	strut-and-tie model
TO	topology optimization
SSI	soil–structure interaction
$d_t, d_c$	concrete damage variables
$E_0$	initial elastic stiffness of concrete
$H_s$	active depth zone
$p, q$	uniform area and line load
$\mu$	coefficient of friction
$L, W$	length, width of a substructure
$D, B$	depth and width of beams
$F_m, F_u$	strut-and-tie member/nodal forces
$l_m$	lengths of struts and ties
$\varepsilon_m$	strain in struts and ties
$M$	total strut-and-tie members
$\phi_v, \phi_f$	strength reduction factors
$A_s, A_{st}, A_{sc}$	area of steel reinforcements
$f_{sy}$	yield strength of steel reinforcement
$w_n, w_r$	nodal zone width, required width
$l_b$	horizontal width of nodal zone
$w_t$	thickness of nodal zone
$\theta_{stm}$	angle of struts and ties
$f'_c, f_{cu}$	concrete, factored $C$ strength
$L_{sy.tb}, L_{sy.t}$	basic/reduced development length
$k_1, k_2, k_3, k_4, k_5$	development length factors
$d_b$	diameter of reinforcing bar
$\beta_s, K$	strut-and-tie factors
$A_{tr}, A_{tr.min}$	transverse, minimum reinforcement
$L_{DE}$	dapped-end notch length
$nex, nely$	number of elements in x and y axes
$xv, yv$	void in the design domain
$volfrac$	volume of fraction of solids
$penal, rmin$	penalizing power, filter size
$C, T$	compression and tension

## ORCID

Bertrand Teodosio  <https://orcid.org/0000-0002-3909-4054>

Kasun Shanaka Kristombu Baduge  <https://orcid.org/0000-0001-5183-701X>

## REFERENCES

- O'Neill D, Organ S. A literature review of the evolution of British prefabricated low-rise housing. *Struct Surv.* 2016;34:191–214.
- Buntrock D. Prefabricated housing in Japan. Abingdon, Oxon and New York: Offsite Architecture: Constructing the future; 2017. p. 190.
- Alonso-Zandari, S, Hashemi, A, Prefabrication in the UK housing construction industry. 5th International Conference on Zero Energy Mass Customised Housing-ZEMCH; 2016; pp. 347–360.
- Rahman MM. The Australian housing market—understanding the causes and effects of rising prices. *Policy Stud.* 2010;31:577–90.
- Daly G. Prefabricated housing Australia: skill deficiencies and workplace practice. Melbourne: International Specialised Skills Institute; 2009.
- Gibb AG. Off-site fabrication: prefabrication, pre-assembly and modularisation. New York: John Wiley & Sons; 1999.
- van Dijk S, Tenpierik M, van den Dobbelsteen A. Continuing the building's cycles: a literature review and analysis of current systems theories in comparison with the theory of cradle to cradle. *Resour Conserv Recycl.* 2014;82:21–34.
- Lichtenberg, J. Slimbouwen: a strategy for efficient and sustainable building innovation. *Construction in the XXI Century: Local and Global Challenges, Symposium Proceedings, CIB W065/N055/W086*; October 2006 Rome, 2006; pp. 206–207.
- Teodosio B, Baduge KSK, Mendis P, Heath D. Prefabrication of substructures for single-detached dwellings on reactive soils: a review of existing systems and design challenges. *Aust J Civ Eng.* 2019;17(2):120–133.
- Teodosio, B, Shanaka, K, Baduge, K, Mendis, P. An optimized prefabricated raft footing system for houses on shrink-swell soils: preliminary results. *Modular and Offsite Construction (MOC) Summit Proceedings*; (2019); pp. 59–66.
- Pujadas-Gispert E, Sanjuan-Delmás D, de la Fuente A, Moonen SF, Josa A. Environmental analysis of concrete deep foundations: influence of prefabrication, concrete strength, and design codes. *J Clean Prod.* 2019;244:118751.
- Pujadas-Gispert E, Sanjuan-Delmás D, Josa A. Environmental analysis of building shallow foundations: the influence of prefabrication, typology, and structural design codes. *J Clean Prod.* 2018;186:407–17.
- Pujadas Gispert, E, Duran, JIDL, Moonen, F. Prefabricated foundations for 3d modular housing. *Changing Needs, Adaptive Buildings, Smart Cities: Proceedings of the Thirty-ninth World Congress on Housing Science, 39 IAHS: volume 2, PoliScript*; 2013; pp. 267–274.
- James MP, Yu B, Martin B. Handbook for the design of modular structures. Clayton, Victoria, Australia: Monash University; 2017.
- Liang, QQ, Xie, YM, Steven, GP, Topology optimization of strut-and-tie models in reinforced concrete structures using an evolutionary procedure [PhD thesis], American Concrete Institute; 2000.
- Adebar P, Kuchma D, Collins MP. Strut-and-tie models for the design of pile caps: an experimental study. *ACI Struct J.* 1990; 87:81–92.
- Schlaich J, Schafer K. Design and detailing of structural concrete using strut-and-tie models. *Struct Eng.* 1991;69:113–25.
- Cook WD, Mitchell D. Studies of disturbed regions near discontinuities in reinforced concrete members. *Struct J.* 1988;85:206–16.
- Hwang S-J, Lee H-J. Strength prediction for discontinuity regions by softened strut-and-tie model. *J Struct Eng.* 2002;128:1519–26.
- Liang QQ, Uy B, Steven GP. Performance-based optimization for strut-tie modeling of structural concrete. *J Struct Eng.* 2002; 128:815–23.
- Hsu TT. Toward a unified nomenclature for reinforced-concrete theory. *J Struct Eng.* 1996;122:275–83.
- Briard J-L, Abdelmalak R, Zhang X, Magbo C. Stiffened slab-on-grade on shrink-swell soil: new design method. *J Geotech Geoenviron Eng.* 2016;142:04016017.

23. Abdelmalak RI. Soil structure interaction for shrink-swell soils “a new design procedure for foundation slabs on shrink-swell soils”, Texas A&M University, College Station, Texas; 2007.
24. Teodosio B, Pauwels VR, Loheide SP, Daly E. Relationship between root water uptake and soil respiration: a modeling perspective. *J Geophys Res Biogeosci.* 2017;122: 1954–68.
25. Teodosio B. Carbon dioxide fluxes between land and atmosphere in catchments with contrasting land cover. Clayton, Victoria, Australia: Monash University; 2017.
26. Li J, Cameron DA, Ren G. Case study and back analysis of a residential building damaged by expansive soils. *Comput Geotech.* 2014;56:89–99.
27. Cameron D. The extent of soil desiccation near trees in a semi-arid environment. *Unsaturated soil concepts and their application in geotechnical practice.* Norwell, MA: Springer; 2001. p. 357–70.
28. Teodosio B, Baduge SK, Mendis P, Heath D. Soil-structure interaction design methods for residential structures on reactive soils. *Australian Structural Engineering Conference: ASEC 2018, Engineers Australia;* 2018, p. 49.
29. Standards Australia. AS 2870-2011: residential slabs and footings, Australian standard; 2011.
30. Korkmaz HH, Tankut T. Performance of a precast concrete beam-to-beam connection subject to reversed cyclic loading. *Eng Struct.* 2005;27:1392–407.
31. International Federation for Structural Concrete. *Structural connections for precast concrete buildings*, CEB-FIP; 2005.
32. Building and Construction Authority. *Buildable solutions for high-rise residential development.* BCA; 2004.
33. Stupre. *Precast concrete connection detail.* Netherlands: Society for Studies on the use of precast concrete; 1978.
34. Teodosio B, Shanaka K, Baduge K, Mendis P. A review and comparison of design methods for raft substructures on expansive soils. *J Build Eng.* 2021;41:102737.
35. Fraser, R, Wardle, L. *Analysis of stiffened raft foundations on expansive soil;* 1975.
36. Holland JE, Cimino DJ, Lawrance CE, Pitt WG. The behaviour and design of housing slabs on expansive clays. *Expansive soils.* Reston, VA: ASCE; 1980. p. 448–68.
37. Poulos, HG. *Analysis of strip footings on expansive soils.* Technical report; 1983.
38. Lytton, RL. *Design criteria for residential slabs and grillage rafts on reactive clay.* Report prepared for CSIRO, Division of Applied Geomechanics; 1970.
39. Sinha J, Poulos H. Behaviour of stiffened raft foundations. *7th Australia New Zealand Conference on Geomechanics: Geomechanics in a Changing World: Conference Proceedings;* Institution of Engineers, Australia; 1996, p. 704.
40. Li, J, *Analysis and modelling of performance of footings on expansive soils [PhD thesis];* 1996.
41. Totoev YZ, Kleeman PW. An infiltration model to predict suction changes in the soil profile. *Water Resour Res.* 1998;34:1617–22.
42. Fredlund, M, Stiansson, J, Fredlund, D, Vu, H, Thode, R, *Numerical modeling of slab-on-grade foundations.* *Geotechnical Special Publication 147;* 2006; 2121.
43. Wray W, El-Garhy B, Youssef A. Three-dimensional model for moisture and volume changes prediction in expansive soils. *J Geotech Geoenviron Eng.* 2005;131:311–24.
44. El-Garhy B, Wray W. Method for calculating the edge moisture variation distance. *J Geotech Geoenviron Eng.* 2004;130: 945–55.
45. Masia MJ, Totoev YZ, Kleeman PW. Modeling expansive soil movements beneath structures. *J Geotech Geoenviron Eng.* 2004;130:572–9.
46. Dafalla MA, Al-Shamrani MA, Puppala AJ, Ali HE. Design guide for rigid foundation systems on expansive soils. *Int J Geomech.* 2011;12:528–36.
47. Shams MA, Shahin MA, Ismail MA. Numerical analysis of slab foundations on reactive soils incorporating sand cushions. *Comput Geotech.* 2019;112:218–29.
48. Shams MA, Shahin MA, Ismail MA. Simulating the behaviour of reactive soils and slab foundations using hydro-mechanical finite element modelling incorporating soil suction and moisture changes. *Comput Geotech.* 2018;98:17–34.
49. Zhang X, Briaud J-L. Coupled water content method for shrink and swell predictions. *Int J Pavement Eng.* 2010;11:13–23.
50. Zhang, X, *Consolidation theories for saturated-unsaturated soils and numerical simulation of residential buildings on expansive soils [Ph.D. thesis],* Texas A&M University; 2005.
51. Teodosio B, Baduge KSK, Mendis P. Simulating reactive soil and substructure interaction using a simplified hydro-mechanical finite element model dependent on soil saturation, suction and moisture-swelling relationship. *Comp Geotech.* 2020;119:1–18.
52. Weerasinghe D, Kodikara J, Bui H. Impact of seasonal swell/shrink behavior of soil on buried water pipe failures, *International Conference on Geotechnical Engineering,* Colombo, Sri Lanka; 2015.
53. Mata-Falcón J, Pallarés L, Miguel PF. Proposal and experimental validation of simplified strut-and-tie models on dapped-end beams. *Eng Struct.* 2019;183:594–609.
54. Weerasinghe, D. *A failure analysis of small-diameter cast iron pipes in reactive soil zones of Melbourne [Ph.D. thesis];* 2018.
55. Kim S, Ahn J, Teodosio B, Shin H. Numerical analysis of infiltration in permeable pavement system considering unsaturated characteristics. *J Korean Soc Disaster Inform.* 2015;11:318–28.
56. Rutqvist J, Börgesson L, Chijimatsu M, Kobayashi A, Jing L, Nguyen T, et al. Thermohydromechanics of partially saturated geological media: governing equations and formulation of four finite element models. *Int J Rock Mech Min Sci.* 2001;38:105–27.
57. Hillerborg A, Modéer M, Petersson P-E. Analysis of crack formation and crack growth in concrete by means of fracture mechanics and finite elements. *Cem Concr Res.* 1976;6:773–81.
58. Teodosio, B. *Design enhancement and prefabrication of raft footings on clayey ground susceptible to reactive soil damage [Ph.D. thesis],* The University of Melbourne; 2020.
59. Hafezolzhorani M, Hejazi F, Vaghei R, Jaafar MSB, Karimzade K. Simplified damage plasticity model for concrete. *Struct Eng Int.* 2017;27:68–78.
60. Andreassen E, Clausen A, Schevenels M, Lazarov BS, Sigmund O. Efficient topology optimization in matlab using 88 lines of code. *Struct Multidiscip Optim.* 2011;43:1–16.

61. Prasad NN. Verification of simplified optimum designs for reinforced concrete beams, University of Southern Queensland, Darling Heights, Queensland, Australia; 2011.
62. Bendsøe MP. Optimal shape design as a material distribution problem. *Struct Opt*. 1989;1:193–202.
63. Sigmund O. A 99 line topology optimization code written in matlab. *Struct Multidiscipl Optim*. 2001;21:120–7.
64. Darwin D, Dolan CW, Nilson AH. Design of concrete structures. New York: McGraw-Hill Education; 2016.
65. Standards Australia, AS 3600-2018: Concrete structures, SAI Global; 2018.
66. Fragomeni, S., van Staden, R.. Design of reinforced concrete corbels using as 3600-2009; 2014.
67. Reineck, K.-H. Modeling structural concrete with strut-and-tie models—summarizing discussion of the examples as per Appendix A of ACI 318-02; Special Publication 208; 2002; pp. 225–242.
68. Dassault Systèmes. Abaqus 6.14: Online documentation help, theory manual; 2016.
69. Al-Rub RKA, Kim S-M. Computational applications of a coupled plasticity-damage constitutive model for simulating plain concrete fracture. *Eng Fract Mech*. 2010;77:1577–603.
70. Tyau JS. Finite element modeling of reinforced concrete using 3-dimensional solid elements with discrete rebar. Provo, Utah; Brigham Young University; 2009.
71. Wilden H. PCI design handbook: precast and prestressed concrete. Chicago, IL: Precast/Prestressed Concrete Institute; 2010.
72. Ousaleem H, Ishikawa Y, Kimura H, Kusaka T, Yanagisawa N, Okamoto K. Seismic performance and flexural stiffness variation of assembled precast high-strength concrete beam jointed at mid-span using transverse bolts. *J Adv Concrete Technol*. 2009;7:205–16.
73. Zou J. Assessment of the reactivity of expansive soil in Melbourne metropolitan area. Melbourne, Victoria, Australia: Royal Melbourne Institute of Technology; 2015.
74. Standards Australia, AS 1289.3.6.1 2009. Standard method of analysis by sieving in methods of testing soils for engineering purposes; SAI Global; 2009.
75. Schaap MG, Leij FJ, Van Genuchten MT. Rosetta: a computer program for estimating soil hydraulic parameters with hierarchical pedotransfer functions. *J Hydrol*. 2001; 251:163–76.
76. Li J, Zou J, Bayetto P, Barker N. Shrink-swell index database for Melbourne. *Aust Geomech J*. 2016;51:61–76.
77. Mata-Falcón, JM. Estudio del comportamiento en servicio y rotura de los apoyos a media madera [PhD thesis], Universitat Politècnica de València; 2015.
78. European Committee for Standardization (CEN), Eurocode 2. Design of concrete structures—part 1-1: General rules and rules for buildings, EN 1992-1-1; 2014.
79. Commonwealth Securities Limited. Economic insights, Australia home size hits 20-year low; 2017.
80. Gould SJ, Kodikara J, Rajeev P, Zhao X-L, Burn S. A void ratio–water content–net stress model for environmentally stabilized expansive soils. *Can Geotech J*. 2011;48:867–77.
81. Tripathy S, Rao KSS. Cyclic swell–shrink behaviour of a compacted expansive soil. *Geotech Geol Eng*. 2009;27: 89–103.
82. Bishop AW. The principle of effective stress. *Teknisk Ukeblad*. 1959;39:859–63.
83. Fredlund DG, Rahardjo H. Soil mechanics for unsaturated soils. Toronto, Canada: John Wiley & Sons; 1993.
84. Forchheimer P. Wasserbewegung durch boden. *Z Ver Deutsch, Ing*. 1901;45:1782–8.
85. Mitchell JK, Hooper DR, Campenella RG. Permeability of compacted clay. *J Soil Mech Found Div*. 1965;91:41–66.
86. Van Genuchten MT. A closed-form equation for predicting the hydraulic conductivity of unsaturated soils 1. *Soil Sci Soc Am J*. 1980;44:892–8.
87. Lubliner J, Oliver J, Oller S, Oñate E. A plastic-damage model for concrete. *Int J Solids Struct*. 1989;25:299–326.
88. Lee J, Fenves GL. Plastic-damage model for cyclic loading of concrete structures. *J Eng Mech*. 1998;124:892–900.

## AUTHOR BIOGRAPHIES



**Bertrand Teodosio**, Research Fellow, Victoria University, Institute of Sustainable Industries and Liveable Cities, D668D/E 70/104 Ballarat Rd, Footscray 3011, Victoria, Australia. Email: [bertrand.teodosio@vu.edu.au](mailto:bertrand.teodosio@vu.edu.au)



**Kasun Shanaka Kristombu Baduge**, Research Fellow, The University of Melbourne, Department of Infrastructure Engineering, The University of Melbourne, Parkville 3010, Victoria, Australia. Email: [kasun.kristombu@unimelb.edu.au](mailto:kasun.kristombu@unimelb.edu.au)



**Priyan Mendis**, Professor, The University of Melbourne, Department of Infrastructure Engineering, The University of Melbourne, Parkville 3010, Victoria, Australia. Email: [pamendis@unimelb.edu.au](mailto:pamendis@unimelb.edu.au)

**How to cite this article:** Teodosio B, Baduge KSK, Mendis P. Design of prefabricated footing connection using a coupled hydro-mechanical finite element model. *Structural Concrete*. 2022;23:2669–95. <https://doi.org/10.1002/suco.202100315>

## APPENDIX A: DETAILS OF THE HYDROMECHANICAL MODEL BY TEODOSIO ET AL.<sup>51</sup> AND A SAMPLE ABAQUS INPUT FILE FOR SOIL–STRUCTURE INTERACTION (SSI) ANALYSES

### Simplified hydromechanical finite element model

A reactive soil mass is modeled as a three-phase elastic material to analyze an unsaturated porous medium. The soil mass consists of solid grains of soil, wetting fluid (i.e., pore water), and nonwetting fluid (i.e., pore air).<sup>54,55</sup> The total soil strain change ( $\varepsilon_T$ ) due to the effects of extrinsic factors is modeled as,<sup>68</sup>

$$\varepsilon_T = \varepsilon_{es} + \varepsilon_{ms}, \quad (A1)$$

where  $\varepsilon_{es}$  is the volumetric strain driven by soil effective stress and  $\varepsilon_{ms}$  is the volumetric strain dependent on the saturation-moisture swelling relationship.

The behavior of a mechanically-stabilized reactive soil mass that underwent a series of shrink-swell cycles<sup>80,81</sup> is determined using Bishop<sup>82</sup>

$$\sigma = \sigma' - S\psi_w. \quad (A2)$$

where  $\sigma$  is the total stress due to mechanical loads applied,  $\sigma'$  is the effective stress,  $\psi_w$  is the pore water pressure, and  $S$  is the degree of saturation of the soil. The resulting incremental coupled hydro-mechanical constitutive stress–strain law was taken as specified in Equation (A1). The shear behavior of the soil was defined by specifying the Poisson's ratio,  $\nu_{soil}$ . The instantaneous shear modulus,  $G$ , is then obtained using

$$G = \frac{E}{2(1 + \nu_{soil})}, \quad (A3)$$

The deviatoric stress,  $\sigma_{dev}$ , is then written as,

$$d\sigma_{dev} = Gd\varepsilon_{es}. \quad (A4)$$

Equation (A4) is integrated to obtain the total shear stress and total elastic shear strain relationship.

The calculation of  $\varepsilon_{ms}$  requires the moisture diffusion equation, sorption model, and moisture swelling model. The three-dimensional water flow in variably saturated soil is described as,<sup>83</sup>

$$k_u \psi_w \left[ \frac{\partial}{\partial x} \left( \frac{\partial h}{\partial x} \right) + \frac{\partial}{\partial y} \left( \frac{\partial h}{\partial y} \right) + \frac{\partial}{\partial z} \left( \frac{\partial h}{\partial z} \right) \right] = m_{sw} \gamma_w \frac{\partial h}{\partial t}, \quad (A5)$$

where  $k_u$  is the unsaturated soil permeability,  $h$  is the water potential head,  $m_{sw}$  is the slope of the soil-water

characteristic curve (SWCC),  $\gamma_w$  is the unit weight of water, and  $t$  is time.

The formulation of the unsaturated permeability is based on Forchheimer Law,<sup>84</sup> which reads

$$k_u = f_{k_u} k_{sat} = \left( \frac{Q\gamma_w}{\partial(\psi_w)/\partial(L')} \right), \quad (A6)$$

where  $f_{k_u}$  is a factor of permeability dependent on saturation,  $k_{sat}$  is the permeability of fully saturated soils,  $Q$  is the volumetric water flux per unit area of soil,  $\partial(\psi_w)/\partial(L')$  is the change in soil suction per unit length depending on the orthogonal axis being considered and  $\rho_w$  is the density of water. The factor,  $f_{k_u}$ ,<sup>85</sup> can be calculated as,

$$f_{k_u} = S^3. \quad (A7)$$

The sorption model is described by a soil–water characteristic curve, SWCC, which defines the  $S$ – $\psi_w$  relationship within the soil matrix using.<sup>24,86</sup>

$$\theta(\psi_w g^{-1}) = \theta_r + \frac{\theta_s - \theta_r}{(1 + |\alpha\psi_w g^{-1}|^n)^m}, \quad (A8)$$

where  $\theta(\psi_w g^{-1})$  is the volumetric soil moisture content,  $\theta_r$  is the residual volumetric soil moisture content,  $\theta_s$  is the volumetric soil moisture content at saturation,  $\alpha$ ,  $n$  ( $n > 1$ ), and  $m$  are empirical parameters reflecting the SWCC (Figure 3a), with  $m$  calculated as,

$$m = 1 - \frac{1}{n}. \quad (A9)$$

The weight and volume relationship of a soil can be used to transform  $\theta$  to  $S$ , given by,

$$S = \frac{\theta \rho_w G_s}{e \rho_b} = \frac{\omega G_s}{e}, \quad (A10)$$

where  $G_s$  is the specific gravity of solids of the soil,  $e$  is the void ratio, and  $\rho_b$  is the bulk density of the soil. Using Equations (A5), (A6), (A8), and (A10), the time-dependent  $\varepsilon_{ms}$  can then be determined using the moisture swelling model presented in Figure 3b dependent to the corresponding  $S$ .

## APPENDIX B: DETAILS OF THE CDP MODEL BY TEODOSIO<sup>58</sup>

Under uniaxial loading, the stress–strain response remains linear elastic until the values of the failure stresses have attained the tension failure stress ( $\sigma_{t0}$ ) and compression failure stress ( $\sigma_{c0}$ ), presented in Figure 4a,b.

Beyond the tension failure stress,  $\sigma_{t0}$ , micro-cracking appears represented macroscopically through softening response from the stress–strain curves. This leads to strain localization in the concrete. When the compression failure stress has been reached, in between  $\sigma_{c0}$  and the ultimate compression stress ( $\sigma_{cu}$ ), the response is depicted by hardening of the stress–strain curves. Past  $\sigma_{cu}$ , softening of the stress–strain curves can be observed. CDP model assumes that curves can be converted into stress versus plastic-strain curves<sup>87</sup> presented as,

$$\sigma_t = \sigma_t(\tilde{\varepsilon}_t^{pl}, \circ\varepsilon_t^{pl}, T_m, f_i), \quad (A11)$$

$$\sigma_c = \sigma_c(\tilde{\varepsilon}_c^{pl}, \circ\varepsilon_c^{pl}, T_m, f_i), \quad (A12)$$

where  $\tilde{\varepsilon}_t^{pl}$  and  $\tilde{\varepsilon}_c^{pl}$  are the equivalent plastic strains,  $\circ\varepsilon_t^{pl}$  and  $\circ\varepsilon_c^{pl}$  are the equivalent plastic strain rates,  $T_m$  is the temperature of the concrete, and  $f_i$  are other variables being considered.

Deterioration of concrete occurs when unloading from any point on the strain softening plastic regime is performed, as shown in Figure 4. The elastic stiffness ( $E_0$ ) is reduced due to the damage and weakening of the concrete, which is characterized by damage variables  $d_t$  and  $d_c$ <sup>88</sup> for uniaxial tension and compression described as,

$$d_t = d_t(\tilde{\varepsilon}_t^{pl}, T_m, f_i), \quad (A13)$$

$$d_c = d_c(\tilde{\varepsilon}_c^{pl}, T_m, f_i), \quad (A14)$$

where the values of  $d_t$  and  $d_c$  ranges from nil for undamaged concrete to one for concrete with total loss of strength. The stress–strain relationship under uniaxial tension and compression loading can be calculated as,

$$\sigma_t = (1 - d_t)E_0(\varepsilon_t - \varepsilon_t^{pl}), \quad (A15)$$

$$\sigma_c = (1 - d_c)E_0(\varepsilon_c - \varepsilon_c^{pl}). \quad (A16)$$

Further details of CDP model are discussed in Hafezolghorani et al.<sup>59</sup> and Dassault Systèmes.<sup>68</sup>

Contact element analysis was applied to model the soil-structure interaction of reactive soils and raft footings. This methodology determines if the contact between the soil and the substructure are intact or separated with respect to support configuration, friction, and penetration due to the interaction. Further details of the mechanics of contact elements are presented in Dassault Systèmes.<sup>68</sup>